Radar Doppler Polarimetry of Wind Turbines using the S-band PARSAX radar

Yiou Zhou

Technische Universiteit Delft

TU Delft Delft University of Technology

Challenge the future

RADAR DOPPLER POLARIMETRY OF WIND TURBINES USING THE S-BAND PARSAX RADAR

by

Yiou Zhou

in partial fulfillment of the requirements for the degree of

Master of Science
in Electrical Engineering

at the Delft University of Technology,
to be defended publicly on Thursday January 15, 2015 at 10:00 AM.

Supervisor:	Prof. dr. ir. O.A. Krasnov	TU Delft
Thesis committee:	Prof. F. Le Chevalier,	TU Delft
	Dr. H. Driessen,	Thales
	Prof. G.J.M Janssen,	TU Delft

This thesis is confidential and cannot be made public until January 15, 2015.

TU Delft Delft University of Technology

ABSTRACT

Due to the necessity of more sources of renewable wind generated energy, the number of wind turbines in the Netherlands has grown in the past. Unfortunately, big sizes and movements of the blades negatively impact ground-based Doppler radars in the form of Doppler clutter. Such clutter leads to a downgrade of the surveillance radar performance in airplanes and precipitation detection, their parameters estimation. Our goal is to characterize and possibly eliminate the Doppler clutter from the wind turbine, where polarization is used as an important tool to reach this goal.

As Doppler frequency and polarization are key characteristics for this study, a theoretical model based on these characteristics is built to predict the behavior of the rotated rotor blades of the wind turbine which shows promising results for amplitude and phase analysis. To evaluate this model, real measurements have been done with the PARSAX radar, which gives possibility to represent the wind turbine data in Doppler-range domain or Doppler-time domain in terms of amplitudes and phases of all four elements of the polarization scattering matrix. Using orthogonal LFM waveforms for simultaneous polarimetric measurements, despite of huge benefits, has one serious drawback a different residual phases in different polarimetric channels. Testing and analysis of a few algorithms, the use of zero Doppler frequency range profile of phases with different algorithms of phase unwrapping, for their estimation and compensation did not result, unfortunately, in reliable compensation of residual phases. As a result, the analysis of wind turbines clutter has been focused on analysis of amplitude polarization characteristics only.

For an experimental study a wind turbine was selected, which is located in Zoeterwoude near a highway. Such location allows to observe scattering from wind turbine and automotive targets simultaneously at the same range distance, with the possibility of data comparison. The goal of data analysis is to find polarimetric features, which for both types of targets behave differently, there is a possibility to eliminate the clutter from the wind turbine only. For comparative analysis, the absolute terms of the averaged covariance matrix are used in terms of 2D histograms to find differences between the wind turbine and automotive targets. This is done for consecutive time frames, where the results show different and similar behavior depending on the time frame. Another approach is to obtain and compare the so called target Euler parameters, which are related to a physical of the specific target to extend our study, a few polarimetric decomposition techniques (Pauli and $H/\overline{\alpha}$) are used to study feasibility of targets classification.

Using comparative analysis with the covariance matrix, shows great potential with correlation coefficient algorithms in combination with polarization. The results are promising, but vary as the correlation coefficient highly depends on the vehicle and the orientation angle of the blades. The results of direct estimation of Euler parameters and the $H/\overline{\alpha}$ decomposition both show differences between vehicles and blades and therefore potential in distinguishing both targets. Though, the results are affected by the residual phase and therefore additional research is recommended on this problem for better reliability.

ACKNOWLEDGEMENTS

I would like to express my gratitude to my supervisor dr. O.A Krasnov for his expertise and assistance during this thesis. I would like to thank him for the discussions, suggestions and encouragement which helped me to finish the thesis. I would also thank dr. O. Yarovoy for the opportunity to start this thesis and his encouragement, which motivated me to finish it. Appreciation also goes to the committee members for reading my thesis. At last, I want to thank my parents and my sister for their support and encouragement.

Yiou Zhou, BSc.
Delft, The Netherlands
November 2014

Contents

1

INTRODUCTION

This chapter serves as an introduction of the thesis and starts with the problem statement in section 1.1. A short description on the approach is found in section 1.2, while section 1.3 gives a short description on related literature. Finally, section 1.4 gives a description of the rest of the thesis.

1.1. PROBLEM STATEMENT

As the result of higher costs of fossil fuels and global warming threats, the necessity and acceptance of renewable energy has increased. One of those renewable sources is wind generated power, which has recently lead to a growth in deployment of wind turbines to produce electrical power. To improve efficiency and reduce the cost, new modern wind turbines are becoming larger. Nowadays, most wind turbines have a tower with a height of approximately 100 meters with blade lengths of 45 meters which form a circle diameter of 90 meters.

Unfortunately, a new problem is exposed on radar measurement. Strong scatterer components such as the blades rotate with high speeds which results in strong clutter on the Doppler radar in both Doppler frequency and spatial domains. This can be seen in figure 1.1, which shows different time segments of the clutter in Doppler Range domain. Observations show that the Doppler clutter highly depends on the orientation of the blades and thus on the time fragment. Due to the time varying nature, wind turbine clutter could interfere with weather signals, which leads to inaccurate estimation of rain rate and wind intensity. Moreover, wind turbine clutter could negatively impact air traffic control where the probability of detecting a wanted air target is decreased [1].

1.2. APPROACH

A modern wind turbine is a large target that mainly consists of a tower, and three moving rotor blades. The tower has a height of approximately 90 meters and the rotor blades have each a length of approximately 45 meters, where the blades are positioned 120^o from one to another. Combining the rotor blades, they span a diameter of approximately 90 meter as seen in figure 1.2. The main objective is to develop an approach to suppress reflections from wind turbines with other targets. As different targets are studied in this research, radar polarimetry can be used as an important tool to accomplish this.

The concept is simple: The radar transmits electromagnetic waves with a controllable polarization to an object, where the polarization of the reflected wave can change when the incident wave interacts with the object. As a result, the backscattered wave has a different polarization depending on the characteristics of the target. Because the moving blades is the main source of Doppler interference and due to its shape and continuous rotation pattern, it is an interesting target for study. In the simplistic case, the blade has a shape of a long cylinder with a relatively small diameter, which

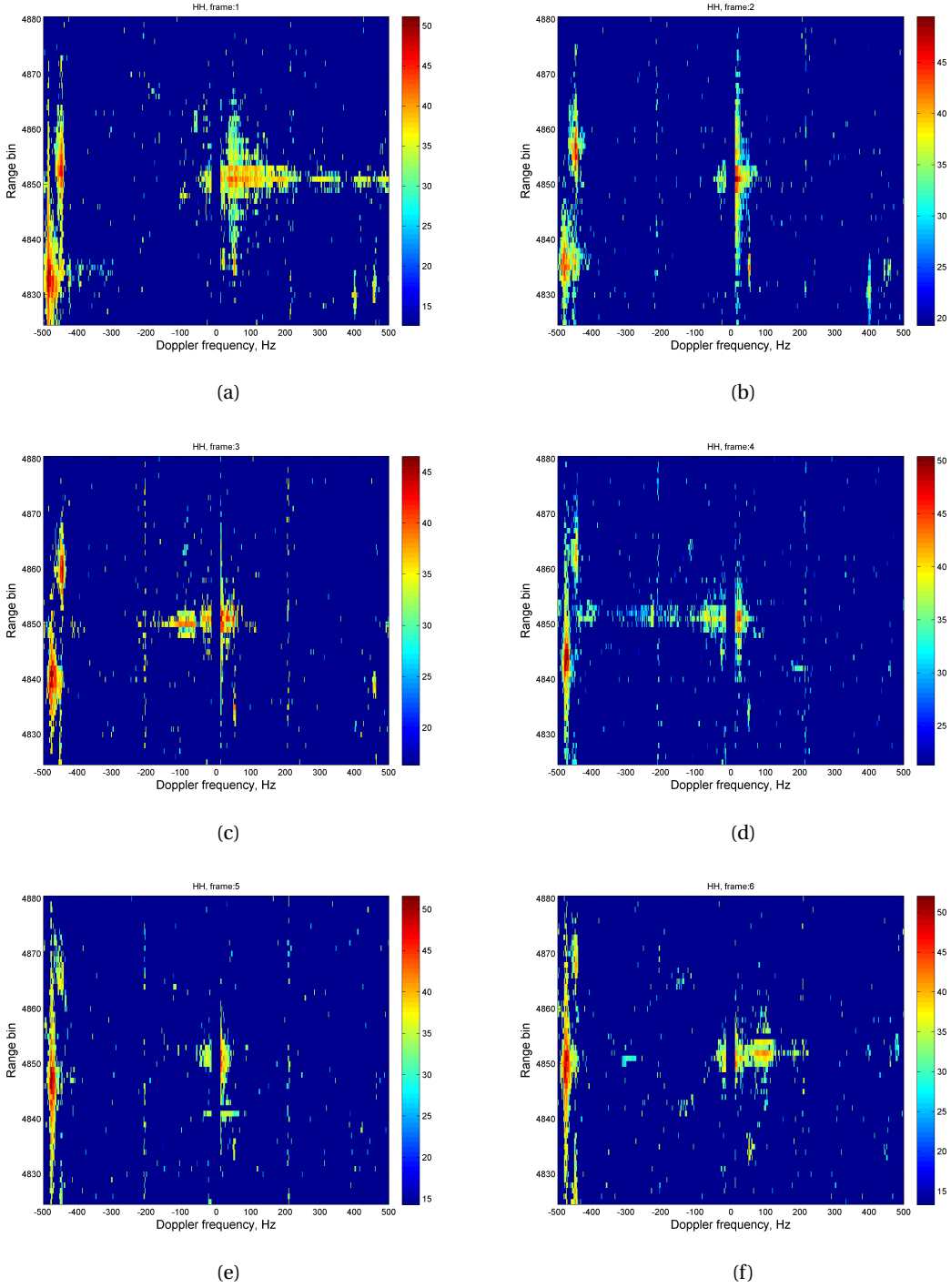

(a) (b) (c) (d) (e) (f)

Figure 1.1: Doppler clutter in six consecutive time frames

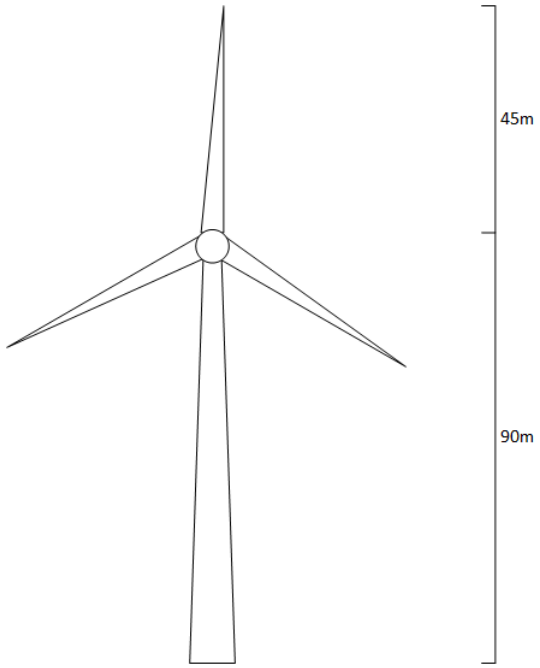

Figure 1.2: Wind turbine

makes it a unique target. When rotation is assumed, the orientation of the blade changes with time which affects the returned signal in polarization and Doppler. Taking into account the periodic nature of the rotation, polarimetric and Doppler study shows great potential to mitigate the clutter from other targets.

To obtain data, measurements have been done by the polarimetric Doppler PARSAX radar located at the Technical university of Delft. Based on polarimetry and Doppler theory, a theoretical model is built to predict the behavior of a rotating blade. Real radar data has been used to validate the model. Intensive study of temporal, micro-Doppler, polarimetric and spatial-temporal statistical characteristics of scattered on wind turbines blades and on other types of moving targets has been done. A few polarimetric decomposition techniques have been applied for real data represented in Range-Doppler and Time-Doppler domains. The goal of such analysis of a big experimental data set was to find most promising measurable features of polarimetric Doppler radar signals to distinguish scattering on wind turbines from other targets and provide information for further development of an algorithm for mitigation of wind-turbines dynamic Doppler clutter.

1.3. OTHER LITERATURE

Some research has been done on this topic. Though, most of the research were to model and predict the Doppler clutter of the blades [2], [3] and [4]. Hence, they do not include polarimetry and provide no method to mitigate the clutter.

1.4. STRUCTURE OF THE THESIS

This thesis consists of 7 chapters, including this introduction as the first chapter. The second chapter gives background information on polarimetry and Doppler theory related to this research. In the third chapter, a theoretical model is built to predict the polarimetric and Doppler behavior of the wind turbine. The fourth chapter describes the measurement set-up, which includes an explanation of the PARSAX radar, the selected wind turbine for this study and limitations of this research. The representation and explanation of the obtained data on the wind turbine is described in the fifth chapter. In the sixth chapter, the methods and results are described and discussed. Conclusions

and further recommendations are presented in the final chapter.

2

BACKGROUND INFORMATION

As radar polarimetry and Doppler theory has much potential to distinguish the wind turbine's blade from other targets, it is crucial to understand the basics. Therefore, this chapter provides a basic overview of polarimetry [5] and Doppler theory. The chapter starts with an explanation of the basics of electromagnetic wave polarization and polarimetry in section 2.1. The scattering matrix of the radar target which relates to the physical object is described in section 2.2. Finally, the Doppler effect is explained in 2.3.

2.1. POLARIZATION

Polarization is an important property of an electromagnetic wave and refers to the changes in the direction of field vectors as it travels. The electromagnetic wave is formed by an electric and a magnetic field, which are perpendicular to the direction of wave propagation and each other. In the following, the polarization of the wave is defined by the electric vector $E(z,t)$. For further analysis the electric field can be represented in the right-handed Cartesian coordination system (x,y,z), where the wave will travel in the z direction. Therefore the electric field can be written in the following formula

$$E(z,t) = \begin{bmatrix} \tilde{E}_x \cos(\omega t - \frac{2\pi}{\lambda} z + \delta_x) \\ \tilde{E}_y \cos(\omega t - \frac{2\pi}{\lambda} z + \delta_y) \end{bmatrix} \tag{2.1}$$

where the $\tilde{\mathrm{E}}_x$ and $\tilde{\mathrm{E}}_y$ stand for the amplitudes of the linear simplistic harmonic oscillations, and the δ_x and δ_y stand for the phases. As shown in figure 2.1, three different types of polarization occur as; linear, circular and elliptical polarization. Linear polarization occurs when the x and y components

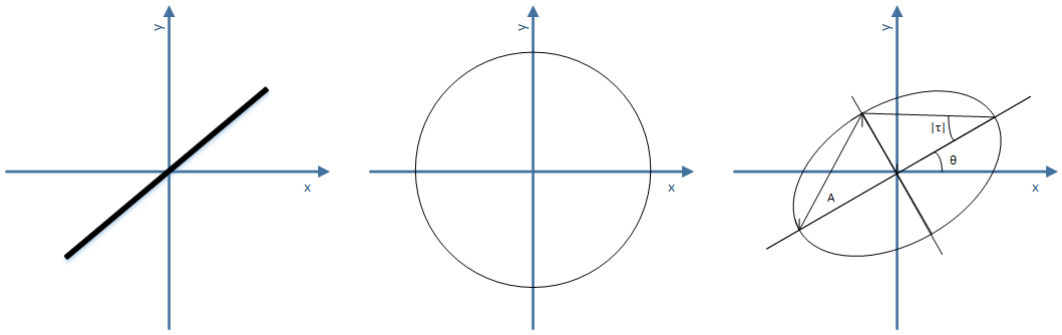

(a) Linear polarization (b) Circular polarization (c) Elliptical polarization

Figure 2.1: Polarization

of the electric field are in phase, where the relative phase between E_x and E_y is either 0 or π. The resulting field is a sine wave that vibrates in a constant direction in the x, y-plane with an angle θ with respect to the x axis. Circular polarization occurs when the magnitudes of both components are equal and the phase difference between both components is an odd multiple of $\frac{\pi}{2}$. The resulting field is a uniform rotation on the x, y-plane that looks like a helix. Elliptical polarization occurs when linear or circular polarization do not occur. As shown in figure 2.1(c), the ellipse highly depends on the amplitude, orientation angle θ and ellipticity $|\tau|$. The orientation angle (θ) is defined as the angled between the ellipse major axis x and takes values between $\frac{\pi}{2}$ and $\frac{\pi}{2}$. The ellipticity (τ) determines the shape of the ellipse and is defined as an angle that ranges between $-\frac{\pi}{4}$ and $\frac{\pi}{4}$.

2.1.1. JONES VECTOR

The Jones vector can be used as matrix to represent all types of polarization of an electric field with the minimum amount of information. The time-space vector $E(z,t)$ seen in equation 2.2 can be written in the following mathematical expression.

$$E(z,t) = \begin{bmatrix} \tilde{E}_x \cos(\omega t - \frac{2\pi}{\lambda} z + \delta_x) \\ \tilde{E}_y \cos(\omega t - \frac{2\pi}{\lambda} z + \delta_y) \end{bmatrix} = \begin{bmatrix} \tilde{E}_x e^{(j\delta_x)} \\ \tilde{E}_x e^{(j\delta_y)} \end{bmatrix} e^{(-j\frac{2\pi}{\lambda} z)} e^{(-j\omega t)} \tag{2.2}$$

Since these components oscillate with the same frequency, the $e^{(-j\omega t)}$ can be omitted.

$$\mathrm{Re}\left[E(z) = e^{(-\frac{2\pi}{\lambda} z)} \right] \tag{2.3}$$

where $E(z)$ is the complex electric field vector. The following step towards the Jones vector is to neglect the spatial information about the wave, as the magnitude of the wave is the same for all points. This is done by substituting $z = 0$ in the complex electric field vector, which leads to the Jones vector

$$\vec{E}(0) = \begin{bmatrix} |E_x| e^{(j\delta_x)} \\ |E_y| e^{(j\delta_y)} \end{bmatrix} \tag{2.4}$$

The resulting Jones vector contains complete information about the amplitudes and phases of the field components. To represent any elliptical polarization, as seen in Figure 2.1(c), the Jones vector can be written as the following equation.

$$\vec{E} = A \begin{bmatrix} \cos(\theta) & -\sin(\theta) \\ \sin(\theta) & \cos(\theta) \end{bmatrix} \begin{bmatrix} \cos(\tau) \\ j\sin(\tau) \end{bmatrix} \tag{2.5}$$

2.2. POLARIMETRIC SCATTERING

Radar stands for Radio Detection and Ranging and is used as a device to transmit an electromagnetic (EM) waves and receive the echoes from the objects within the space of coverage. As the electromagnetic wave travels to the objects within the coverage, where a part of the energy of the waves will be absorbed as the rest will be re-radiated as new waves. It can be used to study characteristics of particular targets, such as aircrafts, ships, vehicles and for this research, wind turbines. Non-polarimetric radars transmit and receive signals with only a single polarization. These radars have the main disadvantage that the signals only measure in one dimension and therefore lose a lot of information on the target. A polarimetric radar transmits and receives with two polarizations, which results in the following four channels

- HH: Transmits horizontal, receives horizontal
- HV: Transmits vertical, receives horizontal
- VH: Transmits horizontal, receives vertical

- VV: Transmits vertical, receives vertical

where both amplitude and phase are measured. Furthermore, there are two cases of radar systems which are

- The monostatic case is the case where the transmitting and receiving antennas are placed at the same location.
- The bistatic case is the case where the transmitting and receiving antennas are in a different location.

Throughout this research, a fully polarimetric monostatic radar has been used. By controlling the polarization of the transmitting wave and measuring the full polarization of the receiving wave, the radar system has obtained more information on the target than when a single polarization has been used.

2.2.1. SCATTERING MATRIX

The scattering matrix is basically a descriptor of the radar cross section of a specific target and describes it's scattering mechanism. When a horizontally polarized wave interacts with a target, the backscattered wave can both get contributions of a horizontal and vertical polarization. As seen in equation 2.4, the Jones vector can be used to completely describe a polarization state of a certain wave. Assuming that the incident and scattered fields can be represented as the Jones vectors, E_i and E_s, the scattering process can be written as the following:

$$\boldsymbol{E_s} = \frac{e^{-jkr}}{r}\boldsymbol{S}\boldsymbol{E_i} = \frac{e^{-jkr}}{r}\begin{bmatrix} S_{HH} & S_{HV} \\ S_{VH} & S_{VV} \end{bmatrix} E_I \tag{2.6}$$

where the scattering matrix is the 2 x 2 matrix and the parameters correspond to the complex scattering coefficients of the target in the far field. Since the diagonal elements relate to the same polarization for the incident and the scattered fields, they are known as the co-polar terms. The off-diagonal terms are known as the cross-polar terms as they relate to the orthogonal polarization states. In the monostatic case, the reciprocity theorem results in equal cross polar terms, where $S_{HV} = S_{VH}$. The term $\frac{e^{-jkr}}{r}$ takes the propagation effects into account, both in amplitude and phase. The scattering matrix contains information on the scattering properties of the target, it can be written as

$$\boldsymbol{E_S} = \begin{bmatrix} |S_{HH}|e^{j\phi_{HH}} & |S_{HV}|e^{j\phi_{HV}} \\ |S_{HV}|e^{j\phi_{HV}} & |S_{VV}|e^{j\phi_{VV}} \end{bmatrix} \tag{2.7}$$

which gives the scattering matrix in amplitudes and phases. As the absolute phase term highly depends on the range of the target, it is almost impossible to accurately measure the absolute phase term. Therefore, relative phase measurement is used where the phase term ϕ_{HH} is factored out as the absolute phase term. This leads to the following scattering matrix for the monostatic case

$$\boldsymbol{E_S} = e^{j\phi_{HH}}\begin{bmatrix} |S_{HH}| & |S_{HV}|e^{j(\phi_{HV}-\phi_{HH})} \\ |S_{HV}|e^{j(\phi_{HV}-\phi_{HH})} & |S_{VV}|e^{j(\phi_{VV}-\phi_{HH})} \end{bmatrix} \tag{2.8}$$

which is now characterized by five parameters: three amplitudes and two relative phases.

2.2.2. RADAR TARGET MATRIX REPRESENTATIONS

In this section some simple scattering matrices are listed in the Cartesian polarization basis, which are described by [6]. For large spheres and flat plates as seen in figure 2.2, the scattering matrix is a unit matrix:

$$\boldsymbol{\Omega} = \begin{bmatrix} 1 & 0 \\ 0 & 1 \end{bmatrix} \tag{2.9}$$

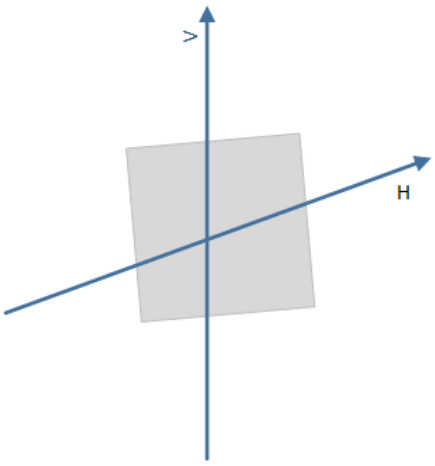

Figure 2.2: Surface

A horizontally aligned dipole, as seen in figure 2.3, has the following scattering matrix

$$\mathbf{\Omega} = \begin{bmatrix} 1 & 0 \\ 0 & 0 \end{bmatrix} \tag{2.10}$$

where the reflected wave is horizontally polarized, without any influence of the incident wave.

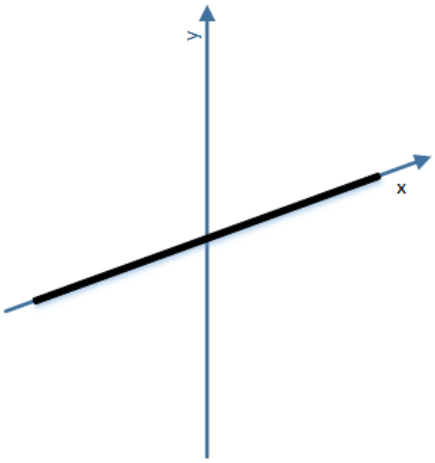

Figure 2.3: Horizontal dipole

When a dipole has an angle θ, a dipole can be considered an oriented dipole where the angle highly influences the following scattering matrix.

$$\dot{\boldsymbol{S}} = \begin{bmatrix} \cos^2(\theta) & \frac{1}{2}\sin(2\theta) \\ \frac{1}{2}\sin(2\theta) & \sin^2(\theta) \end{bmatrix}] \tag{2.11}$$

When θ gradually changes over time, the rotating dipole can be considered as a simplified rotating rotor blade.

When two plates have a relative angle of $\theta = \frac{\pi}{4}$, the target has a two-bounce reflection characteristic. This target is described as dihedral, as seen in figure 2.3 and has the following scattering matrix.

$$\mathbf{\Omega} = \begin{bmatrix} 1 & 0 \\ 0 & -1 \end{bmatrix} \tag{2.12}$$

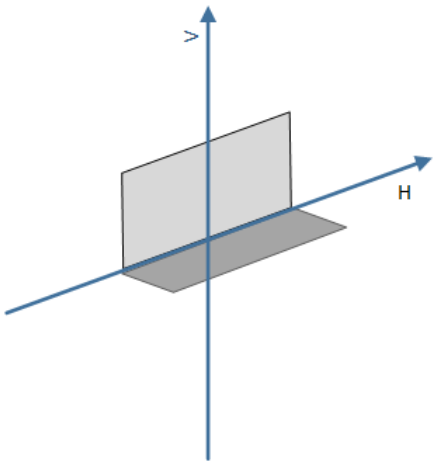

Figure 2.4: Dihedral

2.2.3. RADAR EQUATION

This section explains the interaction between an electromagnetic wave and a given target. The form to describe this phenomenon is called the radar equation [7], as seen in equation 2.13 and explains the relation between the power of the incident electromagnetic wave $\vec{E_i}$ and the power reradiated by the target in the form of the scattered wave E_s.

$$P_r = \frac{P_t G_t A_{ER}}{(4\pi r^2)^2}\sigma \tag{2.13}$$

where P_t is the transmitted power, G_t is the gain of the radar antenna, σ is the radar cross section (RCS) of the target, A_{ER} the effective aperture of the antenna and r is the distance between the object and the radar antenna. The radar cross section (RCS) is a measure on how detectable a target is and can be expressed in the following equation 2.14. The radar cross section depends on a large set of parameters which depend on the system (wave frequency, wave polarization, configuration), but also on the target itself (geometrical structure, dielectric properties). This phenomenon would most likely cause a change in properties in the reradiates waves, where the change of polarization in the re radiated wave can then be used to characterize and identify the target.

$$\sigma = 4\pi r^2 \frac{|\vec{E_S}|^2}{|\vec{E_I}|^2} \tag{2.14}$$

The RCS highly depends on a lot of parameters where the following set of parameters are related to the system

- Wave frequency f
- Wave polarization.
- incident and scattering directions.

The second set of parameters are related to the target.

- Geometrical structure
- Dielectric properties.

The radar equation, shown in equation 2.13 is only valid for point targets. Larger targets, such as a rotor blade are represented as a collection of identical point targets which form the illuminated area A_0. In order to derive the new radar equation of the target, the area must be integrated over A_0 with

$$P_r = \iint_{A_0} \frac{P_t G_t A_{ER}}{(4\pi r^2)^2} \sigma^0 ds \tag{2.15}$$

where σ^0 is the averaged radar cross section and is known as the scattering coefficient. This coefficient is influenced by the ratio of the averaged scattering power density and the incident power density multiplied with the surface of the sphere.

$$\sigma^0 = \frac{<\sigma>}{A_0} = \frac{4\pi r}{A_0} \frac{<|\vec{E}_S|^2>}{|\vec{E}_I|^2} \tag{2.16}$$

where the scattering coefficient is a dimensionless parameter. As the scattering coefficient also depends on the polarization of the incident field and scattered field. Writing the incident field and scattered field as the Jones vector, the scattering matrix seen in equation 2.7 can be related with the RCS in equation 2.13.

2.3. DOPPLER EFFECT

Consider the scenario with a monostatic radar and a rotor blade that is moving towards the radar. The transmitted radiates a continuous wave with carrier frequency f_c

$$s_t(t) = Ae^{j(2\pi f_c t + \phi_0)} \tag{2.17}$$

When the radar interacts with the moving rotor blade, a portion of the transmitted signal is reflected back to the receiver and can be written as

$$s_r(t) = a(t)e^{j(2\pi f_c t + \phi_0 + \Delta\phi(t))} \tag{2.18}$$

where $a(t)$ is the time varying amplitude and $\Delta\phi(t)$ the time-varying phase difference. The phase difference is defined as the ratio of the two way path between the radar and rotor blade and the wavelength multiplied with the scale of the full circle ($2\,\pi$).

$$\Delta\phi(t) = 2\pi \frac{2R}{\lambda_c} = \frac{4\pi R(t)}{\lambda_c} \tag{2.19}$$

where λ_c is the wavelength of the transmitted signal. To obtain the frequency shift, the derivative is taken of the $\Delta\phi(t)$ with respect to the time in the following way

$$\frac{1}{2\pi} \frac{d\Delta\phi}{dt} = f_d = \frac{2\frac{dR}{dt}}{\lambda_c} = \frac{2v_r}{\lambda_c} \tag{2.20}$$

where v_r is the radial speed of the target. When the radial velocity of the target is moving towards the radar, a positive Doppler frequency will occur. On the contrary, a negative Doppler frequency will be observed when the target is moving away from the radar.

2.4. CONCLUSION

As polarimetry and Doppler theory has much potential to distinguish the blade target with other targets, it is crucial to understand the basics. This chapter provided an overview of the basics of polarimetry and Doppler theory which could be helpful for further study.

3

WIND TURBINE MODELING

When the blade is rotating in time, it leads to a continuous changing orientation of the blade. This results in a changing velocity to or from the radar, which inherently leads to a changing Doppler frequency in time. Moreover, polarization properties change as well with a changing blade orientation. This chapter describes two models to predict the Doppler polarimetric behavior of the wind turbine. The first model, shown in section 3.1, describes the Doppler behavior of a simplistic wind turbine where the blades rotate parallel with the line of sight. The second model, shown in section 3.2, presents the changing polarimetric behavior of a wind turbine where the blades rotate perpendicular with the line of sight.

3.1. MICRO-DOPPLER OF WIND TURBINES

In this section a micro-Doppler is produced of a wind turbine with rotating blades which are placed parallel with the line of sight. In order to do this, an assumption is made that the rotor blades can be modeled as a finite length linear wire [8]. Although these assumptions are oversimplified, it still gives a basic prediction on the behavior of the rotor blades in Doppler domain.

3.1.1. RELATIONS FOR AN INFINITESIMAL DIPOLE

To estimate the scattered field from an finite linear wired structure, the structure is sub-divided into a number of infinitesimal dipole with length Δz [9]. As the number of infinitesimal dipoles increases, the length reaches to a length dz. For an infinitesimal dipole with length dz positioned along the z-axis, the electric field can be described as the following.

$$dE_\theta = \frac{j\eta k I_c(x', y, z')e^{-jkR}}{4\pi R}\sin(\theta)dz' \tag{3.1}$$

where R can be defined as $R = \sqrt{(r^2 - rz'\cos(\theta) + z'^2)}$ Using the far-field approximation, R can be simplified as r for amplitude terms and $r - z'\cos(\theta)$. As a result, equation 3.1 can be written as

$$dE_\theta = \frac{j\eta k I_c(x', y, z')e^{-jkr}}{4\pi r}\sin(\theta)e^{-jkz'\cos(\theta)}dz' \tag{3.2}$$

Summing the contributions from all the infinitesimal elements in the limit can be replaced with an integration over the wired construction with length L results in the following field.

$$E_\theta = \int_L dE_\theta = \frac{j\eta k e^{-jkr}}{4\pi r}\sin(\theta)[\int_L I_c(x', y', z')e^{-jkz'\cos(\theta)}]dz' \tag{3.3}$$

The term outside the brackets is called the element factor, which defines the field of a unit length infinitesimal dipole at a reference point. The term inside the brackets is called the space factor, which is a function of the current distribution along the linear wire.

3.1.2. ROTATION AND DOPPLER SPECTRUM

Equation 3.3 in combination with its magnetic counterpart H_θ describes the complex amplitudes of the electromagnetic field with frequency ω. To get a complete description of the EM wave in the time domain, equation 3.3 has to be multiplied with $e^- j\omega t$ Assuming that the linear wire structure is rotating in time, the following case holds $\theta(t) = \theta_0 + \Omega t$. In the element factor, the dependence on angle θ defines the amplitude of the radiated field. In the space factor, the same dependence of the angle θ affects the phase.

For slowly rotating wires, the observation time t is much shorter than the rotation period. From the known serial expansion, the cosine of the space factor can be rewritten as the following Taylor formula

$$\cos(\theta_0 + x) = \cos(\theta_0) - x\sin(\theta_0) - \frac{x^2}{2!}\cos(\theta_0) + ... \tag{3.4}$$

where x = Ωt, the following equation holds

$$e^{-jkz\cos(\theta)(t)}e^{j\omega t} \approx e^{-jkz\cos(\theta_0)}e^{j(\omega-\Omega kz'\sin(\theta_0))t} \tag{3.5}$$

The second term in the right part of equation 3.5 can be seen as the classical Doppler shift.

3.1.3. CASE STUDY

In [8] different case studies have been done to simulate and analyze different rotated linear wired structures, which might be useful to predict the Doppler behavior of rotor blades. A Doppler radar with a wavelength of 10 cm (S-band) has been simulated. The pulse repetition frequency (PRF) is 1 kHz, the processed burst has a length of 128 pulses with zero-padding till 1024 samples for better Doppler representation. The results are presented by using the spectrogram, which shows the results in Doppler frequency and time domain.

NON-SYMMETRICAL LONG DIPOLE

In the first case, a non-symmetrical long dipole as radar reflector is assumed. The electric field is defined with induced current $I_{ind}(x', y', z')$, which is proportional with the tangential component of the incident wave with similar phase shift.

$$I_{ind}(x', y', z') \sim E_\theta(r) * \sin(\theta) * e^{+jkz'\cos(\theta)}dz' \tag{3.6}$$

where the resulting backscattered field is proportional to

$$dE_\theta^{BS}(\theta', z')j\eta\frac{ke^{-jkr}}{4\pi r}E_\theta(r) * \sin^2(\theta) * e^{+j2kz'\cos(\theta)}dz' \tag{3.7}$$

For the non-symmetrical rotating linear wire, the integration has to be done from 0 to L. The resulting Doppler spectrogram for the radar position in the far-field is illustrated in figure 3.1. The maximum Doppler Shifts occurs when the rotating linear wired structure becomes perpendicular to the line of sight, where the frequencies from 0 to the maximum value have the same amplitude. Lower values of amplitudes are seen in the temporal harmonic reflections produced at the ends of the wires.

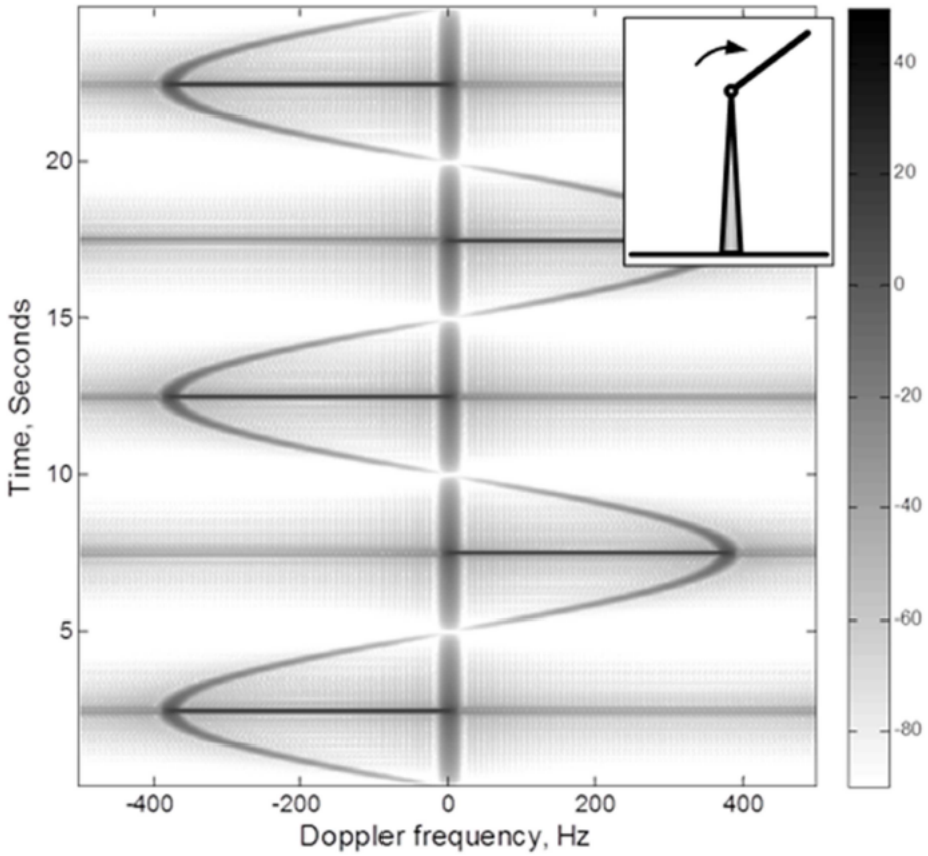

Figure 3.1: Spectrogram of a rotating dipole

WIRED MODEL WITH 3 BLADES

To model a typical wind turbine, a combination of three non-symmetrical linear wires are assumed where the blades are shifted for 120^o one to another. The total scattered field is defined as a sum of fields, where each scattered field from an individual blade of the wind turbine is simulated as

$$E^B S_\theta \sum_n \int_L E_\theta = j\eta \frac{ke^{-jkr}}{4\pi r} \sum_n \sin(\theta_n)[\int_L I_e(x', y', z') e^{+j2kz' \cos(\theta_n)} dz'] \tag{3.8}$$

This equation reflects a simplified case, which assumes that there is no electromagnetic coupling between different construction wires. The spectrogram of the rotating three non-symmetrical linear wires is illustrated in Figure 3.2. The behavior is similar to the non-symmetrical case with two additional wires non-symmetrical wires, which are shifted for 120^o with each other.

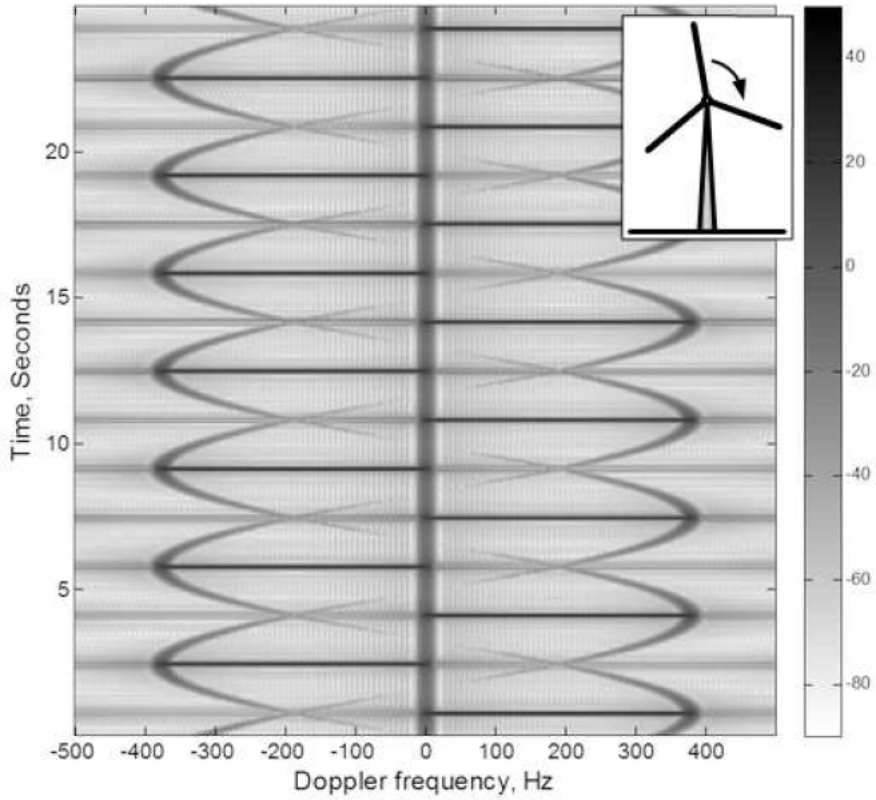

Figure 3.2: Spectrogram of three rotating dipole

3.2. POLARIZATION MODELING

As the blade rotates in time, it affects the polarization characteristics of the blade. In this section, a wind turbine model is built to predict the polarization behavior of rotating blades of the wind turbine. To make such model, a rotating thin dipole is used to simulate a rotating blade to predict the polarimetric behavior. For further reliability of the model, a thick dipole is used to simulate a more realistic blade. Based on these predictions, an algorithm is made to possibly suppress the reflections of the blade.

3.2.1. THIN DIPOLE MODEL

To model a single rotor blade, a thin dipole is considered as a scatterer. Figure 3.3 illustrates a dipole which lies parallel to the x-axis, which results in a horizontally aligned dipole. The horizontal dipole scattering matrix for linear representation can be written as.

$$\boldsymbol{S} = \begin{bmatrix} 1 & 0 \\ 0 & 0 \end{bmatrix} \tag{3.9}$$

where the amplitude of the S_{HH} term is at its maximum. As the rotor blade rotates around the center, a rotation angle θ occurs with respect to the x, y plane, which can be written in the following way.

$$\theta(t) = 2\pi f t \tag{3.10}$$

where t corresponds to the time and f is the frequency, the occurrences of a full rotation per second. As a result of this rotation, the scattering matrix of an oriented dipole is assumed which resembles a simplistic rotating blade. The scattering matrix of an oriented dipole can be obtained by transforming the scattering matrix in equation 3.9 with the rotation matrix.

$$\boldsymbol{S} = R \begin{bmatrix} \cos(\theta) & \sin(\theta) \\ -\sin(\theta) & \cos(\theta) \end{bmatrix} \begin{bmatrix} 1 & 0 \\ 0 & 0 \end{bmatrix} \begin{bmatrix} \cos(\theta) & -\sin(\theta) \\ \sin(\theta) & \cos(\theta) \end{bmatrix} = \begin{bmatrix} \cos^2(\theta) & \frac{1}{2}\sin(2\theta) \\ \frac{1}{2}\sin(2\theta) & \sin^2(\theta) \end{bmatrix} \tag{3.11}$$

Figure 3.4 illustrates the amplitude of the scattering coefficients in time-domain, where all polarization parameters show a sinusoidal function which alternate in strength. When the dipole is vertically aligned ($\theta = \frac{\pi}{2}$), the S_{VV} parameter is at its maximum. When the dipole has an angle of $\theta = \frac{\pi}{4}$, all parameters are equal where the cross polar terms are at its maximum.

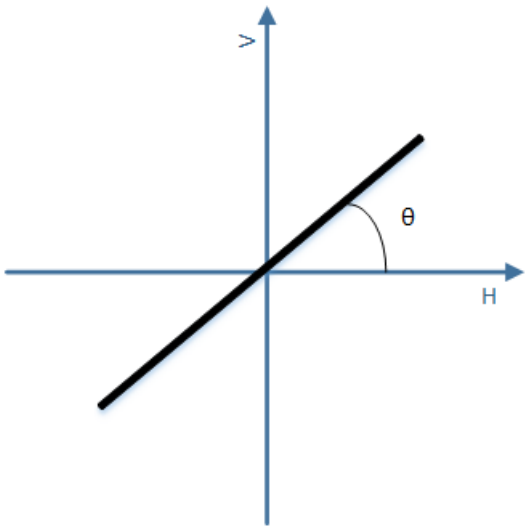

Figure 3.3: Oriented thin dipole

3.2.2. THICK DIPOLE MODEL

For better reliability, the model is extended with a thick dipole for better resemblance with the blade. This is shown in Figure 3.5, where the dipole has a cylindrical form. Considering a horizontal aligned thick dipole, the scattering matrix can be written as the following.

$$\dot{\boldsymbol{S}} = \begin{bmatrix} \dot{\alpha} & 0 \\ 0 & \dot{\beta} \end{bmatrix} \tag{3.12}$$

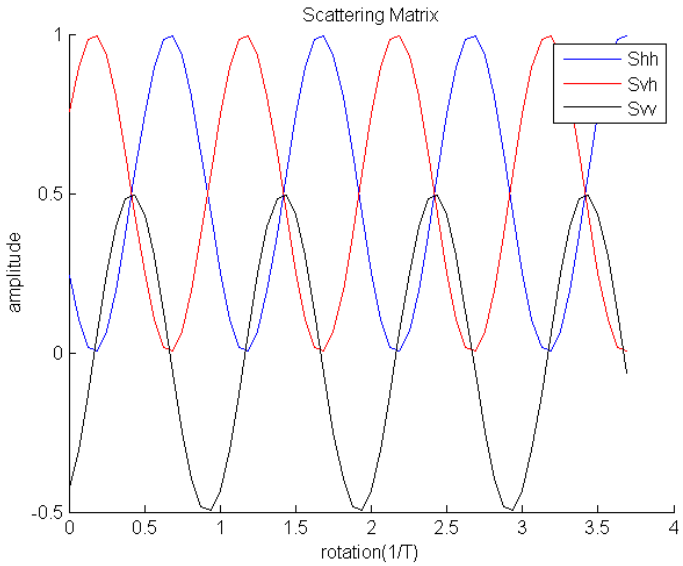

Figure 3.4: Amplitude of the scattering matrix of a rotating thin dipole

where $\alpha > \beta$ and can be any complex number with an maximum absolute value of one. By following this condition, the amplitude of S_{HH} polarization is stronger than that of S_{VV} polarization. Regarding the rotating case, the scattering matrix of the oriented thick dipole shown in Figure 3.5 can be written as

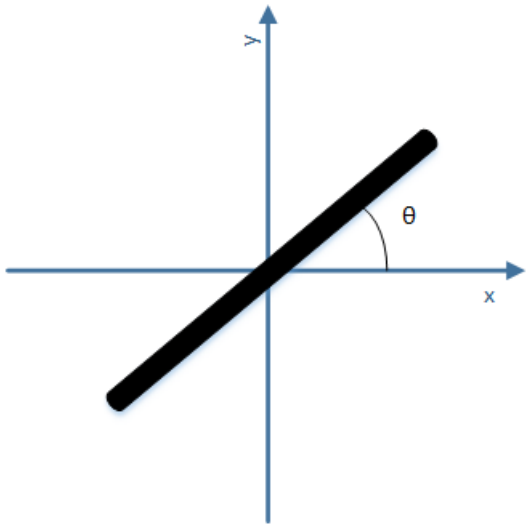

Figure 3.5: Oriented thick dipole

$$\dot{\boldsymbol{S}} = \begin{bmatrix} \cos(\theta) & \sin(\theta) \\ -\sin(\theta) & \cos(\theta) \end{bmatrix} \begin{bmatrix} \dot{\alpha} & 0 \\ 0 & \dot{\beta} \end{bmatrix} \begin{bmatrix} \cos(\theta) & -\sin(\theta) \\ \sin(\theta) & \cos(\theta) \end{bmatrix} = \alpha \begin{bmatrix} \cos^2(\theta) + \frac{\dot{\beta}}{\dot{\alpha}} \sin^2(\theta) & (\frac{\dot{\beta}}{\dot{\alpha}} - 1)\frac{1}{2}\sin(2\theta) \\ (\frac{\dot{\beta}}{\dot{\alpha}} - 1)\frac{1}{2}\sin(2\theta) & \frac{\dot{\beta}}{\dot{\alpha}} \cos^2(\theta) + \sin^2(\theta) \end{bmatrix} \tag{3.13}$$

For the new parameters of the scattering matrix, each parameter has a new period of π, which corresponds to a half rotation of the rotor blade. The values of the complex parameters of the scattering matrix are highly dependent on α and β. In the following section, some possible values of $\dot{\alpha}$ and $\dot{\beta}$ are chosen to study effect on the scattering matrix. For further simplification, $\dot{\alpha}$ and $\dot{\beta}$ can be written as a new term.

$$\frac{\dot{\beta}}{\dot{\alpha}} = \dot{\rho} = \rho e^{-j\Delta\phi} \tag{3.14}$$

where ρ has a maximum value of one. $\Delta\phi$ has a value between $-\pi$ and π and stands for the phase difference between the α and β component. Several cases will be discussed to analyze the parameters of the scattering matrix. Case 1: $|\rho|e^{j\phi} = 0.1$

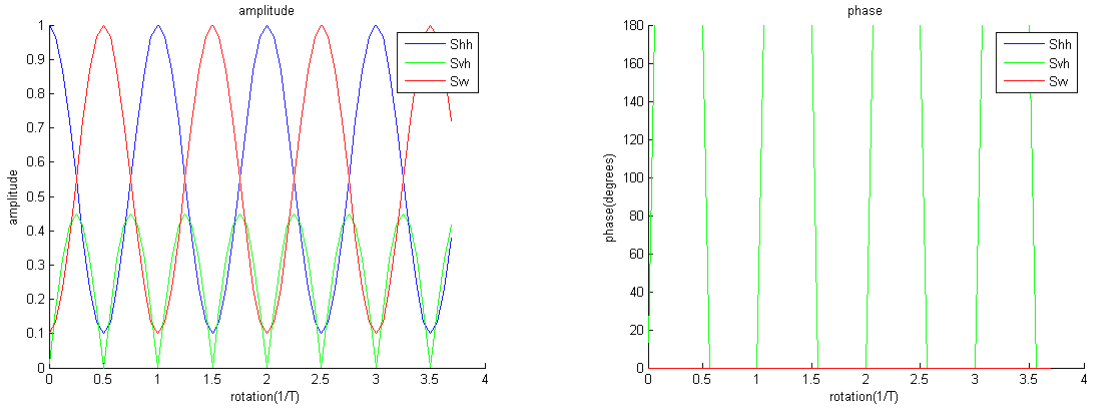

(a) Amplitude of the scattering matrix parameters of case 1

(b) Phase of the scattering matrix parameters of case 1

Figure 3.6: Simulation results of case 1

Case 2: $|\rho|e^{j\phi} = 0.2e^{j\frac{\pi}{4}}$

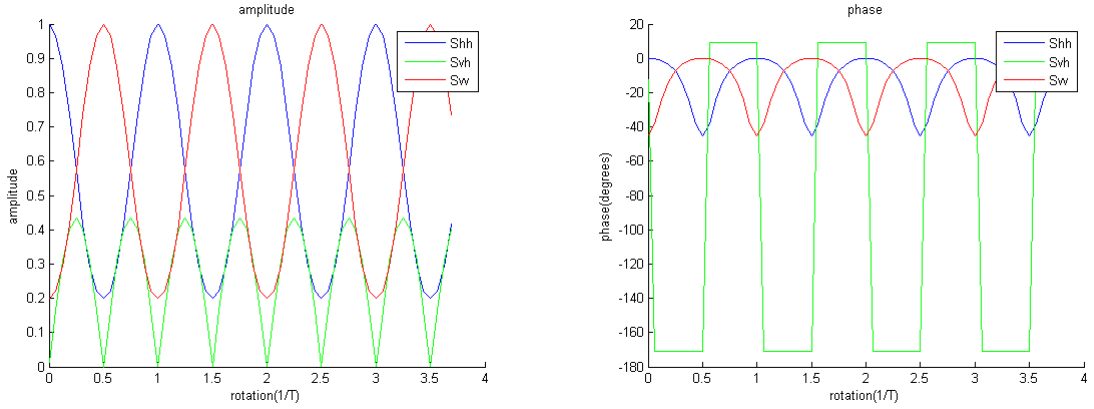

(a) Amplitude of the scattering matrix parameters of case 2

(b) Phase of the scattering matrix parameters of case 2

Figure 3.7: Simulation results of case 2

From Figure 3.6(a) and 3.7(a) it can be seen that the amplitudes are oscillating. When the thick dipole is vertically polarized ($\theta = \frac{pi}{4}$), the amplitude of S_{VV} is higher than the amplitude of S_{HH} polarization. This difference in amplitude becomes stronger when $\alpha >> \beta$. Furthermore, the amplitude of S_{HV} and S_{VH} polarizations is relatively weaker, but has a significant value when $\theta = \frac{\pi}{4}$. Figure 3.6(b) - 3.7(b) illustrate the phase part of the rotated thick dipole, which highly depend on the phase of α and β. Similarly to the amplitude, the phase of all scattering elements show oscillations in time. These consistent oscillations in amplitude and phase show great potential for further amplitude and phase study.

3.2.3. THREE DIPOLE WIND TURBINE MODEL

In this section our model will be extended to the case of three dipoles. For this case, each dipole has an orientation that is shifted 120° apart from one to another. As for using the initial representation of three rotated dipoles, this will result in a change in the rotation matrices as seen in equation 3.15.

$$\dot{\boldsymbol{S}} = \sum_{i=0}^{2} \begin{bmatrix} \cos(\theta + \frac{2\pi i}{3}) & \sin(\theta + \frac{2\pi i}{3}) \\ -\sin(\theta + \frac{2\pi i}{3}) & \cos(\theta + \frac{2\pi i}{3}) \end{bmatrix} \begin{bmatrix} 1 & 0 \\ 0 & 0 \end{bmatrix} \begin{bmatrix} \cos(\theta + \frac{2\pi i}{3}) & -\sin(\theta + \frac{2\pi i}{3}) \\ \sin(\theta + \frac{2\pi i}{3}) & \cos(\theta + \frac{2\pi i}{3}) \end{bmatrix} \tag{3.15}$$

$$\dot{\boldsymbol{S}} = \sum_{i=0}^{2} \begin{bmatrix} \cos^2(\theta + \frac{2\pi i}{3}) & -\sin(\theta + \frac{2\pi i}{3})\cos(\theta + \frac{2\pi i}{3}) \\ -\sin(2\theta + \frac{2\pi i}{3})\cos(\theta + \frac{2\pi i}{3}) & \sin^2(\theta + \frac{2\pi i}{3}) \end{bmatrix} \tag{3.16}$$

This results in Figure 3.8, where it is seen that the parameters are constant in time. Also note that S_{HH} and S_{VV} have the same value and are both represented as the red line. That the parameters are constant in time can be proved in the following way, by choosing the S_{HH} parameter from equation 3.16.

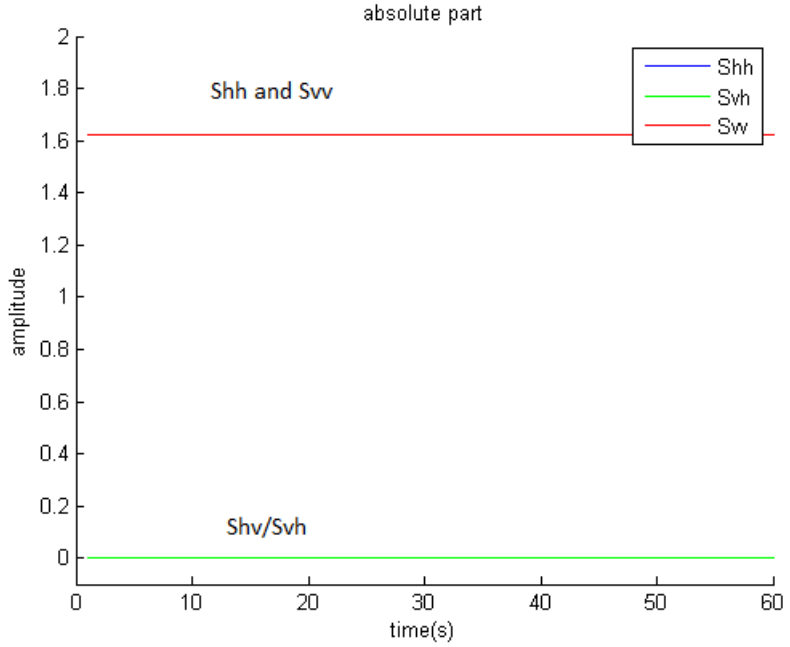

Figure 3.8: Amplitude of three rotating dipole

$$\sum_{i=0}^{2} \cos^2(\theta + \frac{2i\pi}{3}) = \frac{1 + cos(2\theta)}{2} + \frac{1 + \cos(2\theta - \frac{2\pi}{3})}{2} + \frac{1 + \cos(2\theta + \frac{2\pi}{3})}{2} \tag{3.17}$$

Using the following sum-to-product rule

$$\cos(\theta) + \cos(\phi) = 2\cos(\frac{\theta + \phi}{2})\cos(\frac{\theta - \phi}{2}) \tag{3.18}$$

When combining, the sum will result in a constant as seen in Figure 3.8.

$$\sum_{i=0}^{2} \cos^2(\theta + \frac{2i\pi}{3}) = 1.5 + \frac{\cos(2\theta)}{2} + \cos(2\theta)\cos(\frac{2\pi}{3}) = 1.5 \tag{3.19}$$

In conclusion, using three dipoles that are shifted 120^o one to another will result in a constant value for all parameters of the scattering matrix.

3.2.4. PROPOSED ALGORITHM

Using the amplitude of the scattering parameters of the rotating blade found in the model described in section 3.2.2, an algorithm is proposed to possibly distinguish the rotating blade with other targets. By using the oscillating nature of the polarizations in time, correlation studies can be done with correlation coefficient ρ.

$$\rho_{i,j} = \frac{<|S_i * S_j|>}{<|S_i|><|s_j|>} \tag{3.20}$$

where S_i and S_j can be represented as either S_{HH}, S_{HV} or S_{VV} polarization backscattering and <> resembles averaging. Only the amplitude is taken into account. When the amplitudes S_i and S_j are similar, a higher ρ is expected. For the thin dipole case, the amplitude of S_{HH} and S_{VV} polarization show great potential as their amplitude highly depend on the orientation of the dipole. Assume the case of a rotating thin dipole as seen in Figure 3.5, the amplitude of S_{HH} and S_{VV} polarization differ as their peaks and lows appear on different angles. In general, low ρ values are expected. To make such assumptions, a small simulation is made to obtain the ρ values of a thin dipole.

$$\rho_{HHVV} = \frac{<S_{HH}S_{VV}>}{<S_{HH}><S_{VV}>} = \frac{<\sin^2(\theta)\cos^2(\theta)>}{<\sin^2(\theta)><\cos^2(\theta)>} = \frac{1-<\cos(4\theta)>}{2(1-<\cos(2\theta)>^2} \tag{3.21}$$

To obtain the averaged values of the scattering parameters, the following integrals have been used.

$$<\cos(4\theta)> = \int_{\phi_1}^{\phi_2} \cos(4\theta)\,d\theta = \frac{1}{4}\sin(4\theta)\Big|_{\theta_1}^{\theta_2} \tag{3.22a}$$

$$<\cos(2\theta)> = \int_{\theta_1}^{\theta_2} \cos(2\phi)\,d\phi = \frac{1}{2}\sin(2\theta)\Big|_{\theta_1}^{\theta_2} \tag{3.22b}$$

where the integral is taken from starting point θ_1 to ending point θ_2, which relates to the angle of the dipole. Using equation results in the following correlation

$$\rho_{HHVV} = \frac{1-\frac{1}{4}(\sin(4\theta_2)-\sin(4\theta_1))}{2(1-\frac{1}{4}(\sin(2\theta_2)-\sin(2\theta_1))^2)} \tag{3.23}$$

Assuming that θ_1 is the starting point and θ_2 the ending point, the dipole has rotated $\Delta\theta$. Two cases will be discussed here. Case 1 shows different starting angle points θ_1, with increasing $\Delta\theta$, while case 2 shows different $\Delta\theta$ with increasing starting points θ_1. This is shown in Figure 3.9 Depending on the integration interval, the ρ values show some fluctuations as well. In general,

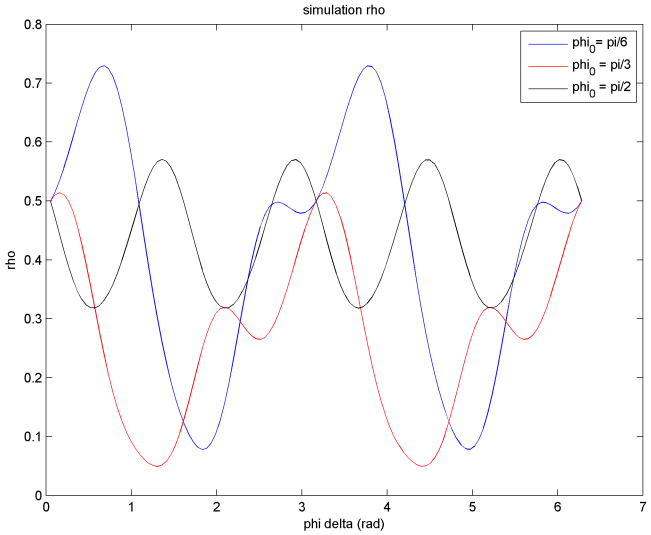

(a) case 1

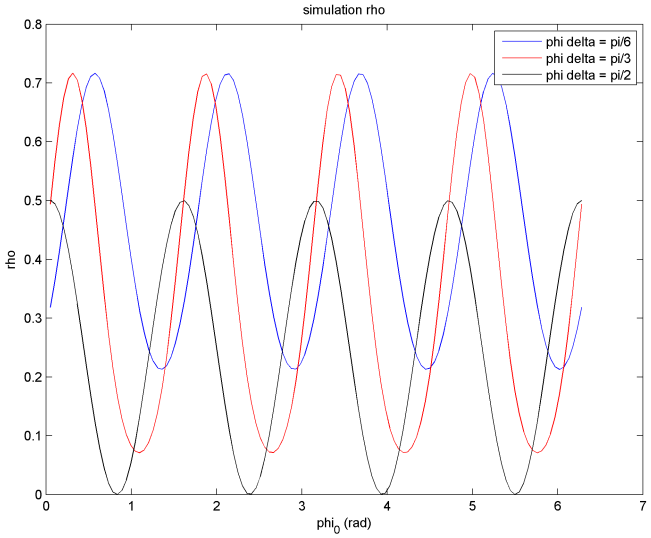

(b) case 2

Figure 3.9: Simulation results

ρ is relatively small and this algorithm has potential in separating rotor blades with stable targets where ρ is expected to be larger.

3.3. CONCLUSION

The first model describes the Doppler behavior of a wind turbine where the blades are modeled as thin wires that rotate parallel with the line of sight. For a single thin wire, the Doppler frequency shows a sinusoidal behavior in time. Observations show stronger reflections and higher Doppler

frequencies when the blades are vertically aligned with the line of sight. The second model shows the polarization behavior of a wind turbine where the blades rotate perpendicular with the line of sight. In time, the scattering parameters present sinusoidal waves where the amplitude and phase of the different polarizations behave differently in time. This shows potential in amplitude and phase study for different polarizations of a rotating blade. Based on the polarimetric model an algorithm is proposed to possibly mitigate the reflections of the blade.

4

MEASUREMENT SETUP

This chapter describes the measurement setup which is used throughout this research to obtain the data. Throughout this research, the PARSAX radar which is a polarimetric Doppler radar is used. This radar is located at the rooftop of the 92 m high building of the faculty of Electrical Engineering at the Technical University of TU Delft as seen in Figure 4.2. The chosen wind turbine for this study is stationed near Zoeterwoude and stands across highway E14 in the Netherlands. This chapter is organized in the following way. Section 4.1 explains the basic operation of the PARSAX radar. Section 4.2 introduces the residual phase problem which poses restrictions in our approach. Finally, section 4.3 describes the wind turbine of interest, which is used to study the Doppler clutter characteristics.

4.1. PARSAX RADAR

The PARSAX radar system is an S-band (3.315 GHz) high-resolution polarimetric Doppler radar and is described in detail in [10]. To obtain range information the radar uses a frequency modulated continuous wave (FM-CW) which makes use of a synchronous linearly frequency modulated (LFM) continuous signal with frequency excursions of B = 50 MHz and time duration of T_s = 1 ms. This is explained in section 4.1.1. To gain polarimetric information, the radar uses a pair of synchronous linearly frequency modulated (LFM) continuous signals with opposite slopes. This principle is explained in 4.1.2.

(a) PARSAX radar (b) map

Figure 4.1: PARSAX radar and map

4.1.1. FM-CW PRINCIPLE

The FM-CW radar makes use of a LFM waveform which consists of a phase function, where the quadratic coefficient α causes a linear frequency over the duration of the signal. The LFM signal can be described as the following phase function

$$s(t) = e^{[j2\pi(f_c t + \frac{1}{2}\alpha t^2)]}, -\frac{T_s}{2} < t \leq \frac{T_s}{2} \tag{4.1}$$

where f_c is the carrier frequency and t is the time variable varying within the pulse-repetition time T_s. The frequency sweep α is equal to the ratio of the bandwidth B and T_s. The instantaneous frequency $f(t)$ obtained in equation 4.2 can be obtained by using the derivative of the argument of the phase function.

$$f(t) = \frac{1}{2\pi}\frac{f_c t + \frac{\alpha t^2}{2}}{dt} = f_c + \alpha t \tag{4.2}$$

When the transmitted signal interacts with an object, the backscattered energy returns to the radar as the received signal. The received signal is a delayed version of the transmitted signal with a time delay τ. This principle is illustrated by Figure 4.2(a) and can be described as the following

$$s_r(t) = e^{(j2\pi(f_c(t-\tau)+\frac{1}{2}\alpha(t-\tau)^2)} \tag{4.3}$$

By mixing it with the conjugated replica of the transmitted signal, only the beat signal remains. This is illustrated in Figure 4.2(b) and can be expressed as

$$s_{beat}(t) = e^{(2\pi(f_c\tau+\alpha\tau t-\frac{1}{2}\alpha\tau^2))} \tag{4.4}$$

where $f_b = \alpha\tau$ is known as the beat frequency which is proportional to the time delay and therefore to the range. After applying a low pass filter, the maximum beat frequency f_b and maximum time delay τ and range are defined. This results in the following boundaries for the beat frequency

$$f_b = \frac{B\tau}{T_s} = \frac{B}{T_s}\frac{2R}{c} \tag{4.5}$$

where c is the speed of light and τ is limited to a maximum range. By applying a Fast Fourier transform on the beat signal, the beat signal can be represented in the frequency domain as seen in Figure 4.2(c). The peak on the particular frequency corresponds to the range of the target. The output consists of 5100 range bins, where each range bin is related to the bandwidth and is defined as

$$\Delta R = \frac{c}{2B} = \frac{cT_s}{2\alpha} \tag{4.6}$$

As B is 50 MHz, ΔR has a resolution of approximately 3 meters and therefore the maximum range is approximately 15 km. To obtain information on the Doppler frequency (velocity) of the target, it can be extracted from phase changes between different sweeps. For this reason, 512 sweeps are used to obtain the information in time-range domain. To obtain the Doppler velocity, a FFT is applied on the time series for all range bins. The maximum unambiguous velocity that can be seen by the radar is defined as

$$V_{max} = \frac{\lambda}{4T_s} \tag{4.7}$$

where λ is the wavelength with a frequency of 3.315 GHz and T_s is the sweep time which has a duration of 1 ms. This would result in a maximum unambiguous velocity of approximately 21.6 m/s, where the velocity resolution depends on the amount of data samples as seen in

$$\Delta V = \frac{2V_{max}}{N} \tag{4.8}$$

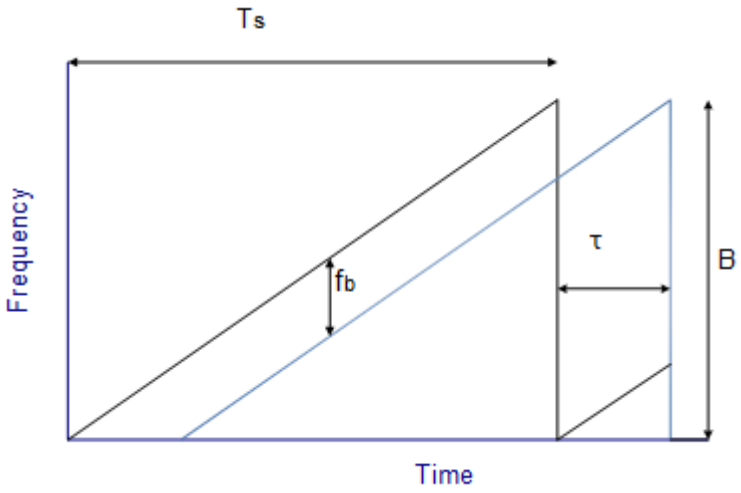

(a) Transmitted and received signals

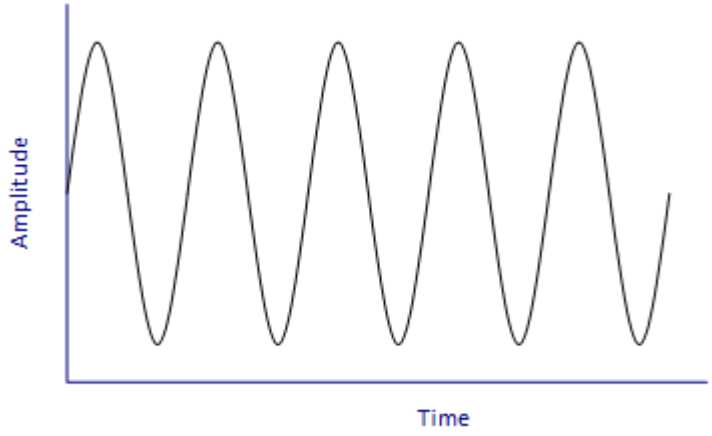

(b) Beat signal in time

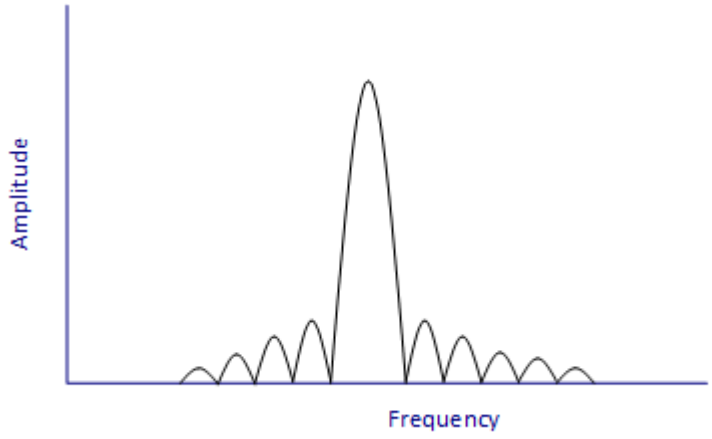

(c) FFT of the beat signal

Figure 4.2: FMCW principle

4.1.2. LFM MODE WITH DUAL ORTHOGONAL SIGNALS

For the PARSAX radar, a scattering matrix measurement is done by using a pair or LFM signals with opposite modulations slopes. The transmitted signal vector consists of two LFM signals with opposite modulation slopes (a up-going LFM and down going LFM) which can then be written as:

$$\vec{\boldsymbol{e}}_{\boldsymbol{t}} = \begin{bmatrix} \dot{e}_{tH}(t) \\ \dot{e}_{tV}(t) \end{bmatrix} = \begin{bmatrix} e^{(j2\pi(f_c t + \frac{1}{2}\alpha t^2))} \\ e^{(j2\pi(f_c t - \frac{1}{2}\alpha t^2))} \end{bmatrix} \quad \frac{-T_s}{2} < t \leq \frac{T_s}{2} \tag{4.9}$$

The received signal is a delayed version of the transmitted one and interacts with the scattering matrix of a certain target and can be written as.

$$\vec{\boldsymbol{e}}_{\boldsymbol{r}} = \begin{bmatrix} \dot{e}_{rH}(t) \\ \dot{e}_{rV}(t) \end{bmatrix} = \begin{bmatrix} \dot{S}_{HH} & \dot{S}_{HV} \\ \dot{S}_{VH} & \dot{S}_{VV} \end{bmatrix} \begin{bmatrix} e^{(j2\pi(f_c(t-\tau) + \frac{1}{2}\alpha(t-\tau)^2))} \\ e^{(j2\pi(f_c(t-\tau) - \frac{1}{2}\alpha(t-\tau)^2))} \end{bmatrix} \tag{4.10}$$

Again, the received signals are mixed and matched with the transmitted conjugate replicas. After low pass filtration and a Fast Fourier transformation, the four parameters of the scattering matrix can be written as a function of the beat frequency. This process can be summarized as the following

$$\begin{bmatrix} \dot{S}_{HH}(f_b) & \dot{S}_{HV}(f_b) \\ \dot{S}_{VH}(f_b) & \dot{S}_{VV}(f_b) \end{bmatrix} = FFT\left[LPF \begin{bmatrix} e_{Hr}(t)e_H^*(t) & e_{Hr}(t)e_V^*(t) \\ e_{Vr}(t)e_H^*(t) & e_{Vr}(t)e_V^*(t) \end{bmatrix} \right] \tag{4.11}$$

4.2. RESIDUAL VIDEO PHASE

Using dual orthogonal LFM signals introduces a new problem, which is the residual phase that contributes an extra phase bias. Using the deramping function used in section 4.1.2, the scattering parameters can be described as the following

$$\begin{aligned} \boldsymbol{\dot{S}_{HH}(f_b)} &= \dot{S}_{HH} e^{[-j2\pi(f_c\tau)]} e^{[j2\pi(-\frac{1}{2}\alpha\tau^2)]} \\ \boldsymbol{\dot{S}_{HV}(f_b)} &= \dot{S}_{HV} e^{[-j2\pi(f_c\tau)]} e^{[j2\pi(\frac{1}{2}\alpha\tau^2)]} \\ \boldsymbol{\dot{S}_{VH}(f_b)} &= \dot{S}_{VH} e^{[-j2\pi(f_c\tau)]} e^{[j2\pi(-\frac{1}{2}\alpha\tau^2)]} \\ \boldsymbol{\dot{S}_{VV}(f_b)} &= \dot{S}_{VV} e^{[-j2\pi(f_c\tau)]} e^{[j2\pi(\frac{1}{2}\alpha\tau^2)]} \end{aligned} \tag{4.12}$$

where the right exponential term represents the residual phase term. Unfortunately, this gives a positive phase bias for S_{HV}/S_{VV} elements and negative phase bias for S_{HH}/S_{VH}. This residual phase is seen in equation 4.13 and is proportional to the range.

$$\Delta\phi_R = \pi\alpha\tau^2 = \pi\frac{B}{T_s}\frac{4R^2}{c^2} \tag{4.13}$$

The scattering matrix which is affected by the residual phase can then be written as

$$S = \begin{bmatrix} \dot{S}_{HH} & \dot{S}_{HV} \\ \dot{S}_{VH} & \dot{S}_{VV} \end{bmatrix} = \begin{bmatrix} S_{HH}e^{j\phi_{HH} - j\Delta\phi_R} & S_{HV}e^{j\phi_{HV} + j\Delta\phi_R} \\ S_{VH}e^{j\phi_{VH} - j\Delta\phi_R} & S_{VV}e^{j\phi_{VV} + j\Delta\phi_R} \end{bmatrix} \tag{4.14}$$

where the scattering parameters are complex and the residual phase gives either a negative or positive phase bias. Assuming reciprocity ($S_{HV}e^{j\phi_{HV}} = S_{VH}e^{j\phi_{VH}}$), the measured residual phase can be obtained with

$$\Delta\phi_R = 0.5 * (j\phi_{HV} - j\phi_{VH}) \tag{4.15}$$

Using equation 4.13, a theoretical prediction can be made of the residual phase where the residual phase is depends on the range. To compare the hypothetical value, the equation 4.15 is used to obtain the residual phase from the measured data for all range bins. For each range bin, the average phase is taken from all time samples to get a rough estimate of the residual phase on that particular range. Also note that the maximum range goes till approximately 15 kilometers, where the residual

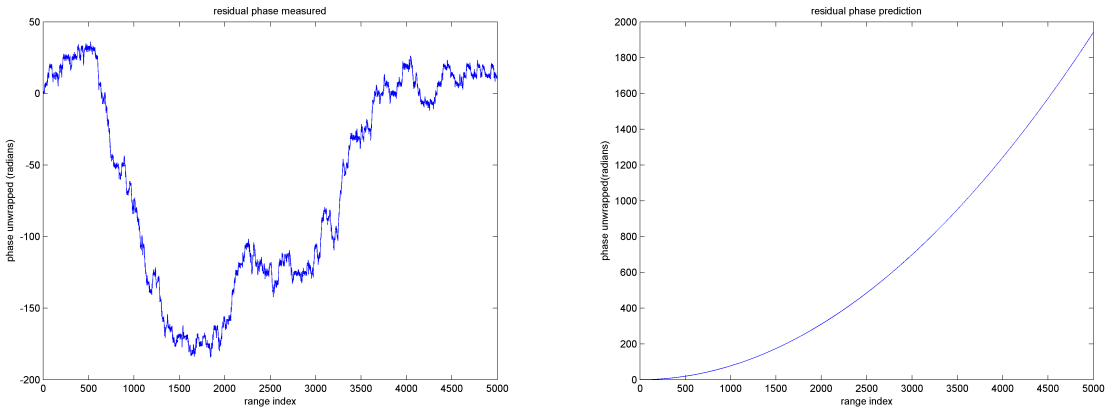

(a) (b)

Figure 4.3: Measured and predicted residual phase

phase increases considerably with higher ranges. For that reason, phase unwrapping is required to efficiently study the phase change between different ranges. Unfortunately, Figure 4.3 shows a contradiction between the predicted and measured residual phase. While the predicted residual phase shows a smooth quadratic curve, the measured residual phase shows strong irregularities between ranges, which could be the result of an absent target or phase noise. Therefore, additional research is recommended to mitigate the residual phase problem.

4.3. CHOSEN WIND TURBINE

A typical wind turbine consist of the following components: A tower, nacelle, rotor and the three rotor blades. The static tower usually has a height of 90 meters and gives a constant zero velocity return. The nacelle is placed on the tower and its RCS (Radar Cross Section) highly depends on the yaw angle of the turbine. The area occupied by the three rotor blades has a diameter of 90 meters, where the rotor blades are moving in a certain velocity. Due to the size and materials of the rotor blades, they can be easily detected by the radar. The amount of Doppler interference highly depends on the yaw angle of the turbine. When the rotor blade area are perpendicular (yaw angle = 90^o) to the line-of-sight, the Doppler effect will be minimal. When the rotor blade area is completely parallel (yaw angle = 0) to the line-of-sight, the Doppler velocity will be at its maximum. The chosen wind turbine is stationed near Zoeterwoude as seen in Figure 4.4 and has a relative distance of approximately 14-15 kilometers. This wind turbine has a rotation speed of approximately 7 rotations per minute and is therefore clearly visible on the Doppler radar. Furthermore, the wind turbine is located near a highway with a variety of vehicles such as trucks and cars. As the cars move in a constant speed, they appear on a constant Doppler frequency. This gives opportunity for polarization comparison between vehicles and blades.

Figure 4.4: Wind turbine, Zoeterwoude

4.4. CONCLUSION

This chapter described the measurement set-up for data acquisition on the wind turbine which includes polarization and Doppler information. These measurements were done by the PARSAX radar located in Delft, where the basic operation is explained in section 4.1. Using the PARSAX radar has a clear disadvantage, as it introduces the residual phase problem. This problem is explained in section 4.2 and is caused by using dual orthogonal LFM waveforms. This leads to a phase bias for different polarizations, which either has to be compensated or poses a limitation in this research. Finally, the wind turbine of interest is described in section 4.3. The wind turbine is stationed near a highway and has a slight yaw angle, where the presence of moving vehicles gives opportunity for comparison study.

5

DATA REPRESENTATION

The obtained data of the PARSAX radar presents the information in time-range domain. In order to identify the data with the movements of the blade, the data has to be processed. This chapter explains the steps to obtain presentable data from the wind turbine and relates it with the rotation of the rotor blades. This chapter starts with section 5.1 which transforms the data in range Doppler domain in consecutive time frames. Another way to present the data is to transform the data as a spectrogram (time-Doppler domain) which is explained in chapter 5.2. Furthermore, a closer study is done on the residual phase problem related to the wind turbine which is described in section 5.3.

5.1. DOPPLER RANGE PROFILES

One way to investigate the polarization of a wind turbine is by using a Range Doppler profile, where certain Doppler frequencies correspond to certain parts of the turbine. To generate such profile, a FFT is applied on the time series with a time window of approximately 0.5 seconds (N = 512 data samples) to transform the data in the Doppler frequency domain.

$$X(k) = \sum_{n=0}^{N-1} x(n) e^{\frac{-j2\pi nk}{N}} \tag{5.1}$$

On the Doppler Range profile, the wind turbine shows reflections on range bin 4847 to 4854, covering approximately 20 meters. Figure 5.1, 5.2 and 5.3 illustrates a series of consecutively range Doppler profiles of a rotating wind turbine in S_{HH}, S_{HV} and S_{VV} polarization, where each profile has a time frame of approximately 0.5 seconds. The Doppler frequency represents the speed of the target and is spread from -500 to 500 Hz (approximately from - 21 m/s to 21 m/s). The sign of the frequency indicates whether the targets are moving towards or removing away from the transmitter. Figure 5.1(a) presents a strong line of multiple scatterers spread from the zero Doppler frequency to the maximum Doppler frequency and represents a (nearly) vertical dipole which is moving towards the transmitter. The parts closer to the center are shown on the lower Doppler frequencies and give relative stronger reflections, while the parts further from the center give relative weaker reflections on higher Doppler frequencies. Objects that move away from the radar are seen on the negative Doppler frequencies. The other two rotor blades that are shifted 120^o from one to another show relative weaker reflections on the negative Doppler frequencies over multiple range bins. On other time fragments in Figure 5.1(b), the reflections are found on lower Doppler frequencies over multiple range bins. Comparing different polarizations in Figures 5.1, 5.2 and 5.3 show that the S_{HH} and S_{VV} polarization show stronger reflections than S_{HV} polarizations. This is more emphasized on lower Doppler frequencies, where the targets are relatively more stable.

5.2. SPECTROGRAM ANALYSIS

One problem with using a Doppler range profile is that each profile has a certain time frame, which removes the possibility to analyze the Doppler polarimetric characteristics within that time frame. This can be resolved by using a spectrogram where the data is given in time-frequency domain, at the cost of spatial information. To get the spectrogram, consider a short-time Fourier transform (STFT) which is given in the following.

$$STFTx[n] = X(m,k) = \sum_{n=-\infty}^{\infty} x[n]w[n-m]e^{\frac{-j2\pi nk}{N_{fft}}} \tag{5.2}$$

where m is the timing index and k is the frequency index. Furthermore, $x[n]$ is the received discrete signal from one particular range bin, N_{fft} is the size of the FFT. The window function has a certain size and is written as $w[n-m]$, where index m determines the position of the window function. The principle is to multiply $x[n]$ with window function $w[n]$ and apply a FFT on the product. This gives the data in frequency domain for a time duration of the window size. By constantly repeating this process with a sliding window, it illustrates how the frequency spectrum changes with time.

- $x[n]$ has a length of 4048 data samples, which corresponds with approximately 4 seconds.
- The window size w is 128 data samples. By choosing a shorter window, a better time resolution is enhanced at the cost of frequency resolution.
- To obtain a better time resolution, consecutive time segments must overlap at the cost of higher complexity. In order to have a decent time resolution and low complexity, the consecutive segments are overlapped with 96 samples (75%). To achieve a better frequency resolution, the size of N_{fft} is set to 1024.

The spectrogram is expressed in dB in the following way

$$P_{dB}(m,k) = 10log|X(m,k)|^2 e^{j\phi(m,k)} \tag{5.3}$$

Where ϕ is the phase. The spectrogram represents the center of the wind turbine in amplitude and is illustrated in Figure 5.4 for one range bin for four different polarizations. The horizontal axis represents the slow time in seconds, the vertical axis represents the Doppler frequency and the color scale corresponds to the power of the signal in dB. The spectrogram shows similarities with the Doppler model in section 3.1, where the strong periodic peaks (at 0 and 3 s) indicate a nearly vertical blade. The peak on the positive Doppler spectrum indicates a blade which is moving towards the radar. The negative counterpart corresponds to a blade that is moving away from the radar. Also note, that the reflections on the positive Doppler frequency are somewhat stronger, which might be the result of double reflections between the blade and tower. On other angles, large chunks of the blade will appear on other range bins. Again, the reflections on the lower Doppler frequencies are in general stronger, and are caused by thicker parts of the blade which appear near the center of the rotation circle. The strong reflections on the zero Doppler frequency are coming from the static tower. The reflections on the higher Doppler frequencies are coming from cars and trucks on the highway. Again, the S_{HH} and S_{VV} polarization are relatively more dominant in comparison with S_{HV} and S_{VH} polarization.

5.3. RESIDUAL PHASE

In section 4.2, the residual phase problem is introduced which was the result of using LFM mode with dual orthogonal signals. This would lead to a range dependent phase bias, which is negative for S_{HH} and positive for S_{VV}. As some range bins do not have an object, this could influence the residual phase analysis. For that reason, this section studies the residual phase effect in the wind turbine region. Considering that the wind turbine is around 14-15 kilometers away, the expected residual phase between range bin 4850 and 4851 is expected to be around 40^o.

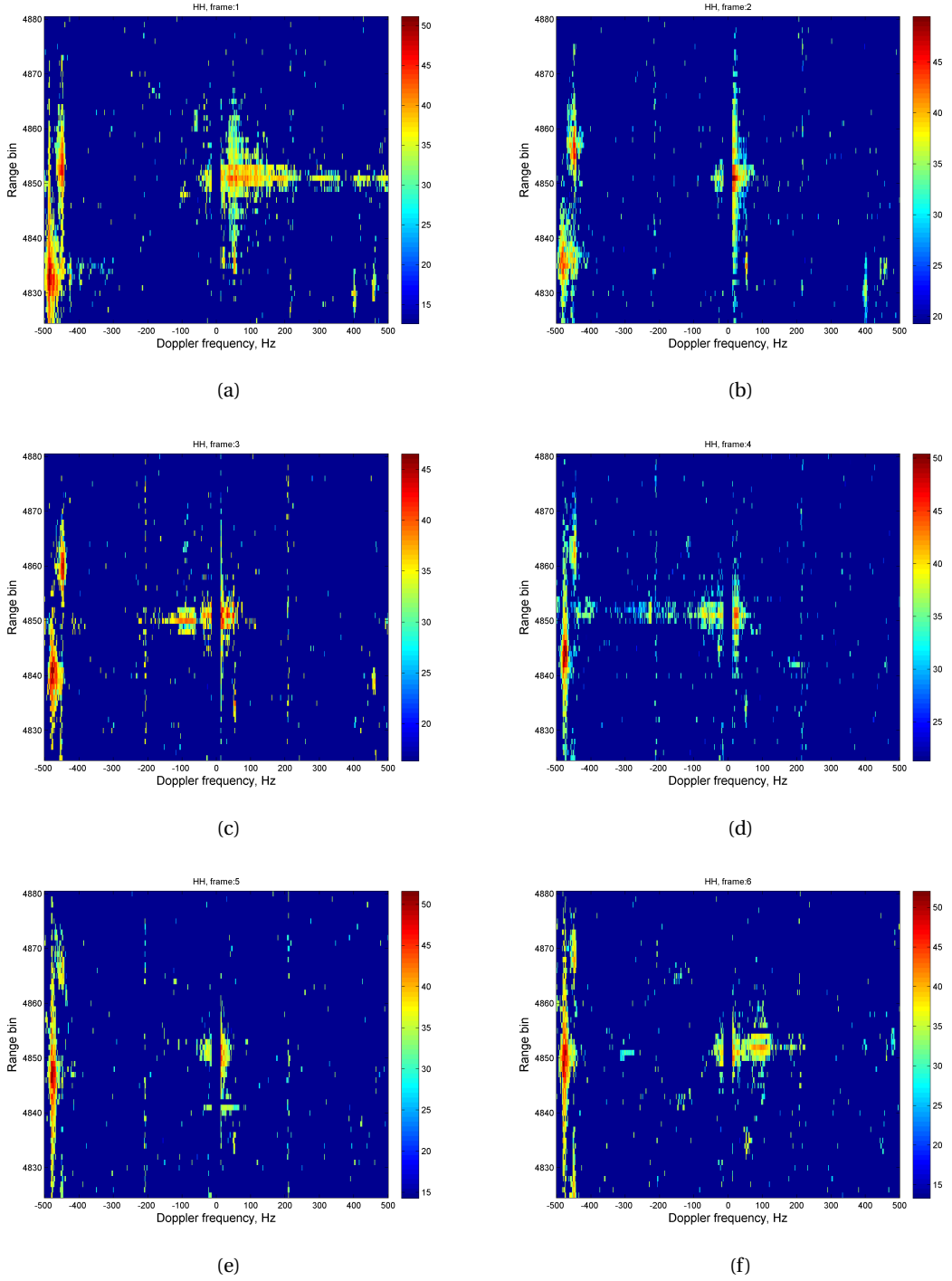

(a) (b) (c) (d) (e) (f)

Figure 5.1: Range Doppler profile in six consecutive time frames for S_{HH} polarization for a wind turbine

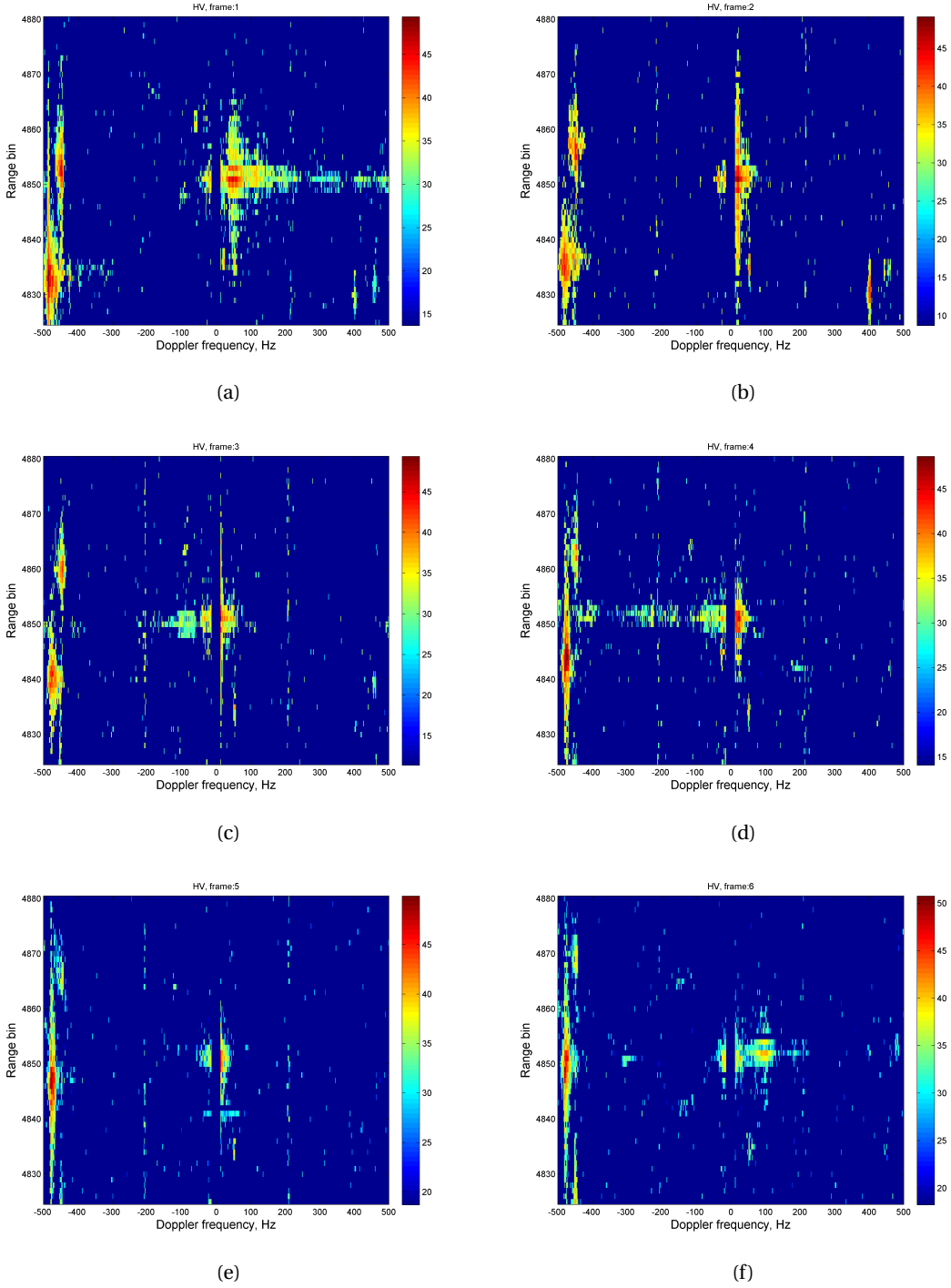

(a) (b) (c) (d) (e) (f)

Figure 5.2: Range Doppler profile in six consecutive time frames for S_{HV} polarization of a wind turbine

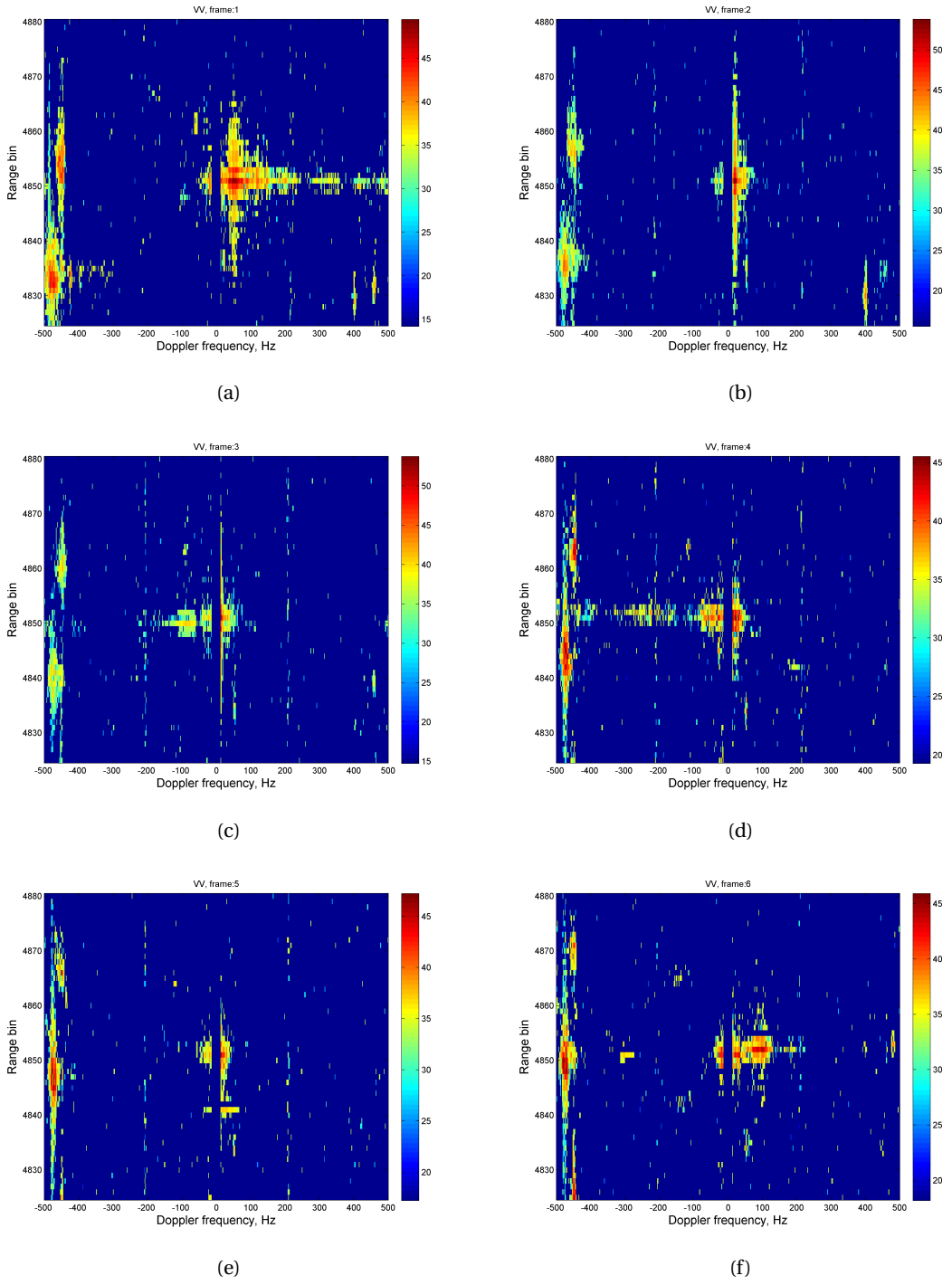

(a) (b) (c) (d) (e) (f)

Figure 5.3: Range Doppler profile in six consecutive time frames for S_{VV} polarization of a wind turbine

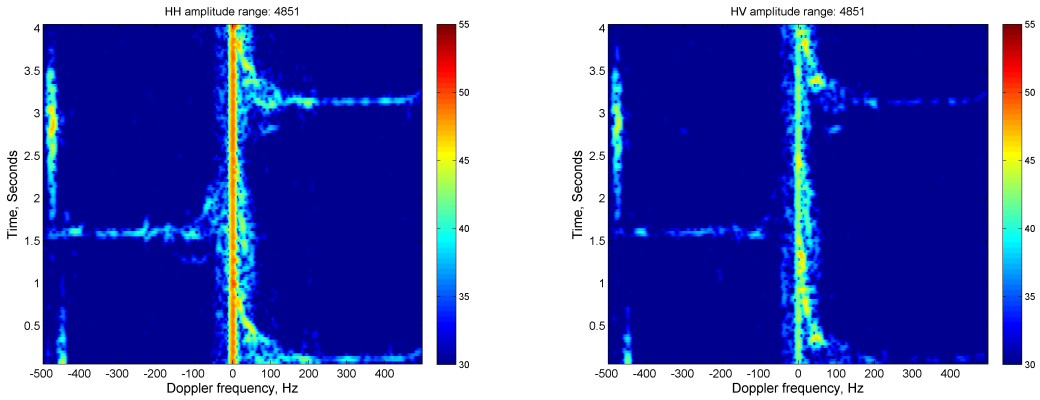

(a) S_{HH} (b) S_{HV}

(c) S_{VH} (d) S_{VV}

Figure 5.4: Spectrogram of the center of the wind turbine in four different polarizations

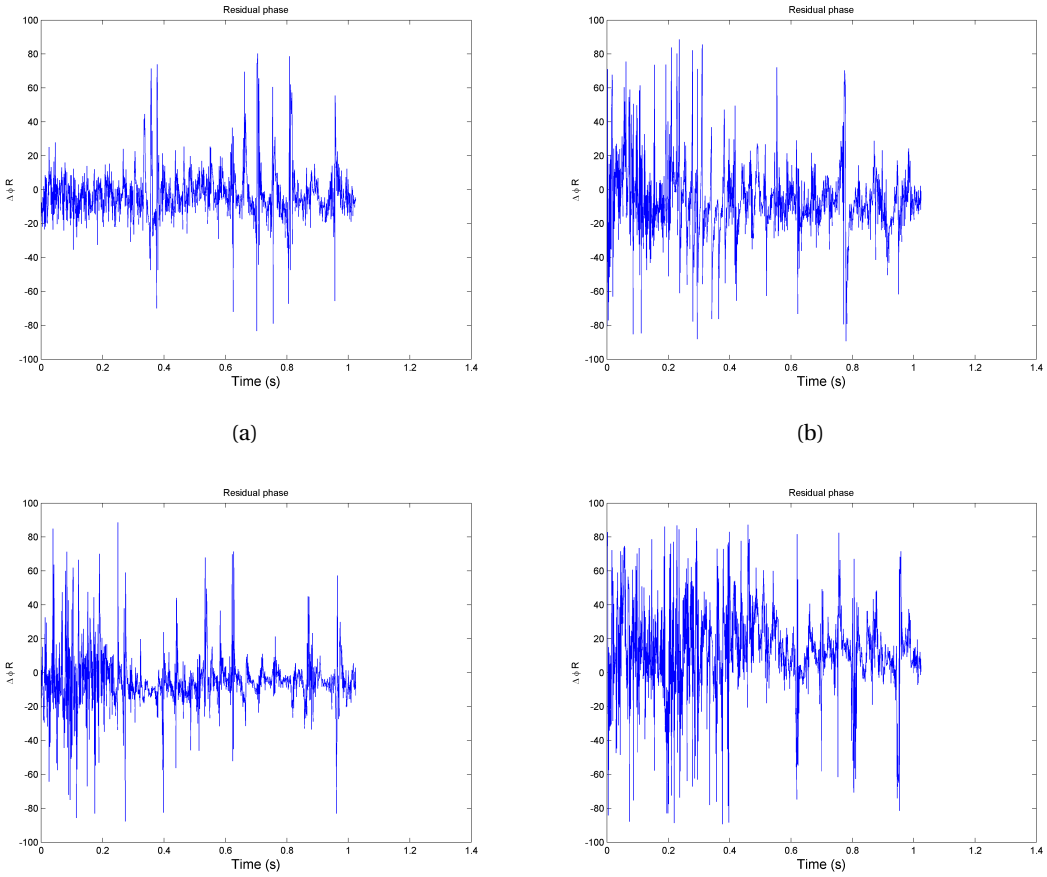

(a) (b)

(c) (d)

Figure 5.5: Residual phase in time domain with increasing range

5.3.1. RESIDUAL PHASE TIME DOMAIN

In this section, the effect of residual phase is observed in time domain as seen in Figure 5.5 with histogram in Figure 5.6. The chosen range bins correspond with the location of the wind turbine. With each increasing range bin, the residual phase is expected to increase with 40^o.

with the related histograms found in Figure 5.6 Residual phase is somewhat stable, but shows some fluctuations as the result of the phase of S_{HV}. Furthermore, the residual phase does not necessarily increase with range. When the phase does increase, it is a lot smaller than the predicted range change.

5.3.2. RESIDUAL PHASE SPECTROGRAM

For further reliability, the residual phase is studied in spectrograms. In Figure 5.7, the residual phase of the wind turbine is obtained with increasing range.

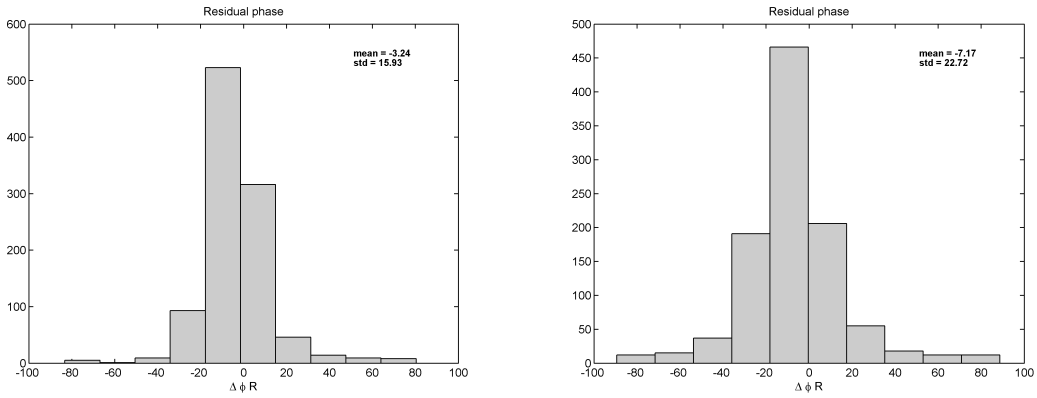

(a)

(b)

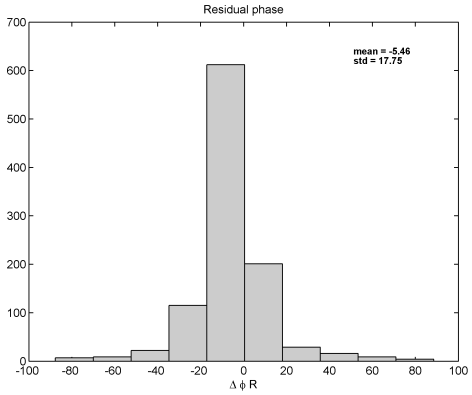

(c)

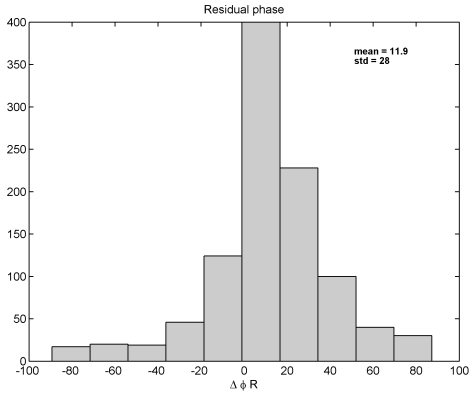

(d)

Figure 5.6: Residual phase in time domain in histogram with increasing range

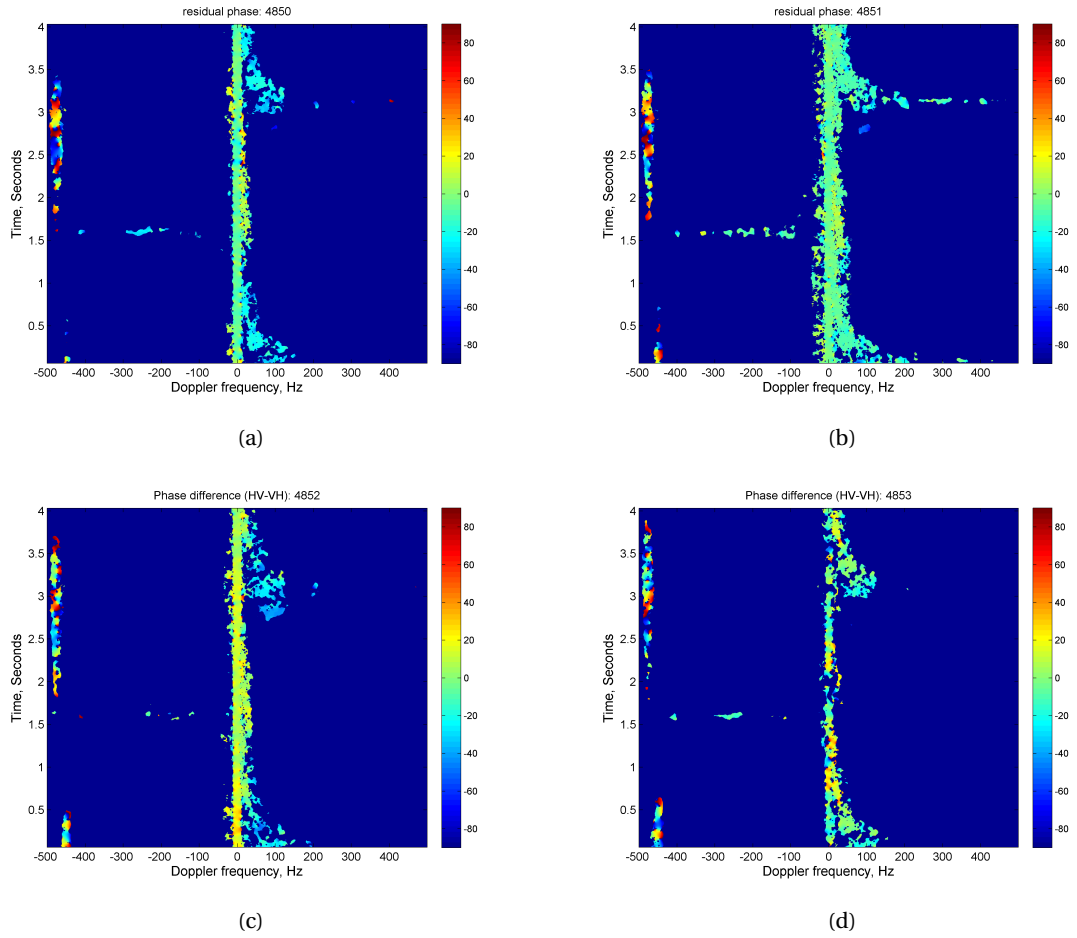

Figure 5.7: Residual phase in spectrogram in four different range bins

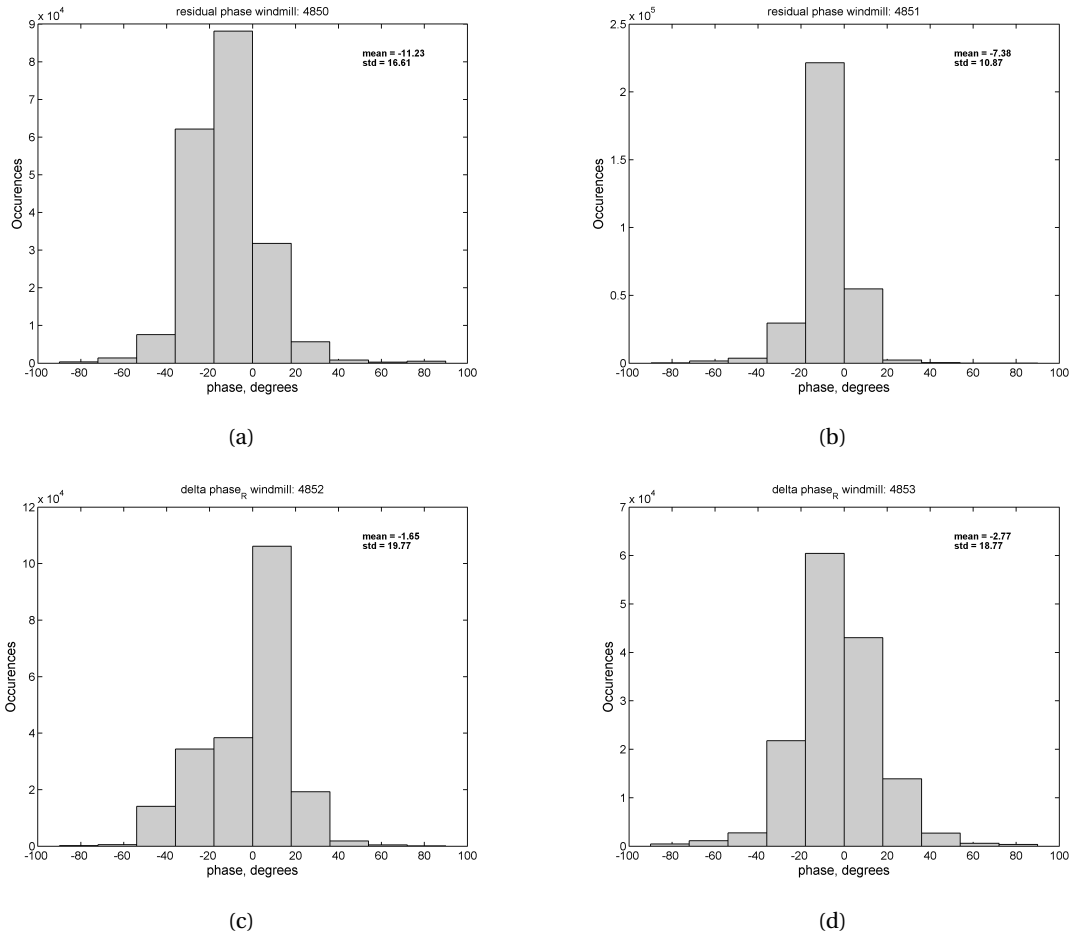

Figure 5.8: Histogram residual phase of the spectrogram of four different range bins

with the histograms found in Figure 5.8. From these figures, it can be seen that the residual phase is slightly different for blades than for the tower. In general, the residual phase does seem to slightly increase with increasing range bin. Unfortunately, it is a lot smaller than the expected residual phase and could not yet be solved. For that reason, this thesis will focus more on amplitude study.

5.3.3. AMPLITUDE CALIBRATION ANALYSIS

For further analysis, amplitude comparison is done between S_{HV} and S_{VH} to verify the monostatic assumption that $S_{HV} = S_{VH}$. To achieve this, the ratio is compared in dB scale for a spectrogram which is shown in Figure 5.9. From this figure, there is some clear amplitude differences between S_{HV} and S_{VH}. This difference is smaller with stronger amplitude as seen in Figure 5.9(b), but still noticeable. Therefore, calibration studies in amplitude is also recommended for further study.

5.4. CONCLUSION

This chapter described data representation and gives the data based on the movements of the chosen wind turbine. The first method described in section 5.1 shows the data in range Doppler domain in consecutive time fragments. The second method described in section 5.2 gives the data as a spectrogram for a single range bin, which is obtained by applying STFT. Furthermore, a study is done on the residual phase relating to the wind turbine which is presented in section 5.2. Unfortunately,

measured data does not agree with the hypothetical values. Therefore, the residual phase problem is not yet resolved and additional research is recommended.

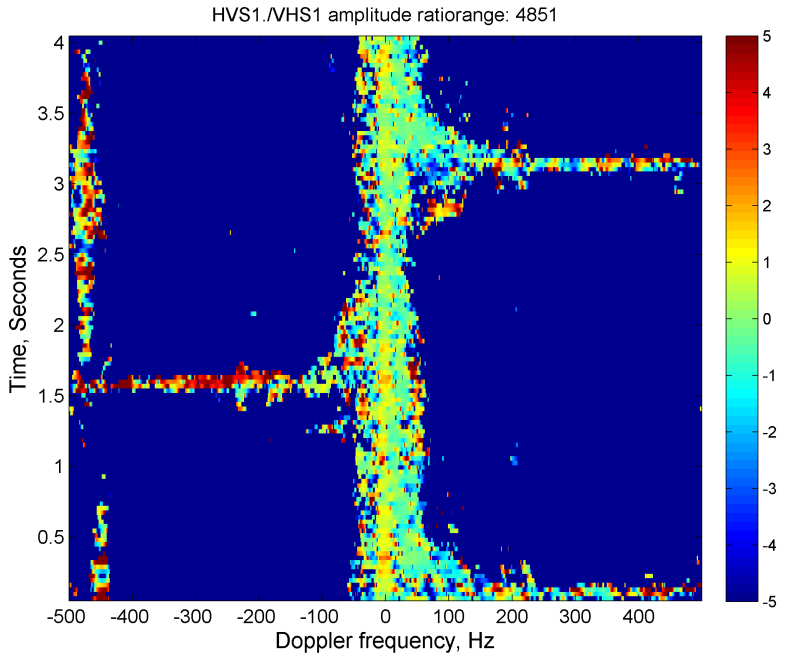

(a)

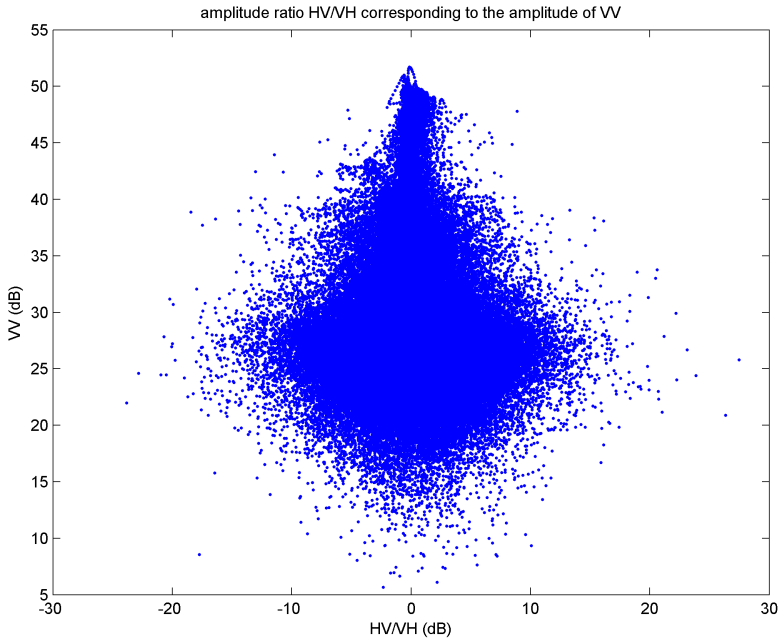

(b)

Figure 5.9: Ratio S_{HV} and S_{VH}

6

RESULTS

This chapter provides results to possibly distinguish the different targets by using the polarimetric data represented in chapter 5. Section 6.1 provides an amplitude study using the covariance matrix to find differences in polarization between rotor blades and vehicles. In section 6.2 the Huynen target characteristics are described, which gives more information on the characteristics of the target. In section 6.3 decomposition results are shown to find possible differences between vehicles and blades.

6.1. COVARIANCE MATRIX ANALYSIS

As the residual phase could not be resolved, more focus will be done on the amplitude analysis. One way to study the amplitude characteristics is by using a covariance matrix which is defined as

$$\boldsymbol{C} = \begin{bmatrix} <|S_{HH}|^2> & <|S_{HH}||S_{HV}|> & <|S_{HH}||S_{VH}|> & <|S_{HH}||S_{VV}|> \\ <|S_{HV}||S_{HH}|> & <|S_{HV}|^2> & <|S_{HV}||S_{VH}|> & <|S_{HV}||S_{VV}|> \\ <|S_{VH}||S_{HH}|> & <|S_{HV}||S_{VH}|> & <|S_{VH}|^2> & <|S_{VH}||S_{VV}|> \\ <|S_{VV}||S_{HH}|> & <|S_{VV}||S_{HV}|> & <|S_{VV}||S_{VH}|> & <|S_{VV}|^2> \end{bmatrix} \tag{6.1}$$

where the <> indicates temporal averaging of resolution cells in space and Doppler domain. In order to classify the targets, averaging is applied on all elements of the covariance matrix. This is done in the following way.

$$< C_{i,j}(k,l) >= \frac{1}{4NM} \sum_{n=k-N}^{k+N} \sum_{m=l-M}^{l+M} (C_{i,j}(n,m)) \tag{6.2}$$

where i and j can be either S_{HH}, S_{HV} or S_{VV}. The parameters N and M define the Doppler and spatial space which is used to average all values into one value that corresponds to the center of this space (k,l). For complete information on the covariance matrix, this process is repeated for all range and Doppler indexes, with a $N = M = 3$. The covariance matrix contains complete information on the amplitude variance and correlation for all the amplitude of the elements of the scattering matrix S. In total, the covariance matrix contains ten independent parameters: four power elements in the main diagonal and six cross correlations in the off-diagonals. For normalization purposes, the individual parameters are normalized with the sum power elements of the averaged covariance matrix given by

$$Span = <|S_{HH}|^2> + <|S_{HV}|^2> + <|S_{VH}|^2> + <|S_{VV}|^2> \tag{6.3}$$

To study the parameters of the covariance matrix, two different targets are considered: The rotor blades and cars. In Figure 6.1, two covariance elements are compared of cars and rotor blades in

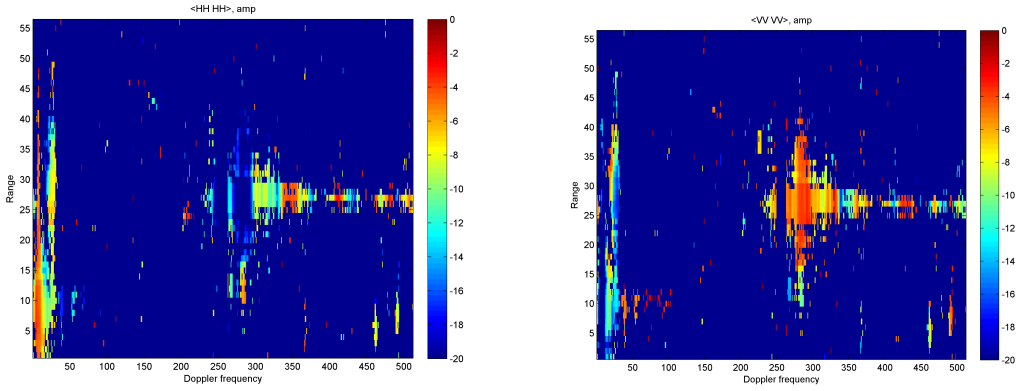

(a) (b)

Figure 6.1: $< |S_{HH}|^2 >$ and $< |S_{VV}|^2 >$

range Doppler domain. It illustrates significant differences in intensity between $< |S_{HH}|^2 >$ and $< |S_{VV}|^2 >$ for cars and rotor blades.

Observing the case of a nearly vertical blade found in Figure 6.1, it can be seen that the intensity of $< |S_{HH}|^2 >$ and $< |S_{VV}|^2 >$ varies in intensity depending on the part of the vertical blade. This slightly contradicts the established thick dipole model made in section, where a single polarization parameter should have dominated the whole vertical blade. This implies that the established thick dipole model in section 3.2.2 is too simplistic and more research should be done to the complex structure of the blade.

6.1.1. 2D HISTOGRAM ANALYSIS

For further analysis, these two parameters are compared in a two dimensional (2D) histogram where both vehicles and rotor blades are analyzed individually. This is done by only extracting the relevant data cells which belong to the specified target. The data cells of the vehicle are taken from a different part of the highway and is therefore taken from different range bins. The histogram presents the spread of the intensity in polarization for one specific time fragments. This is shown in Figure 6.2 (blades) and Figure 6.3 (vehicles), which show histograms of six consecutive time fragments.

Comparing the histograms between vehicles and blades show some similarities. For the wind turbine however, concentrated spreads are seen in particular in Figure 6.2(b). The histograms of the car show a histogram with more randomness, where the intensity is more scattered. To enhance reliability, the Kullback-Leibler Distance is used, which is explained in the following section.

6.1.2. KULLBACK-LEIBLER DISTANCE

When two 2D histograms are compared, a certain measure is to find out the difference between the two distributions. This so called measure is called the Kullback-Leibler Distance[11], which can be written as the following equation.

$$D_{KL}(P||Q) + D_{KL}(P||Q) = \sum_i \sum_j [ln\frac{P(i,j)}{Q(i,j)}P(i,j) + ln\frac{Q(i,j)}{P(i,j)}Q(i,j)] \tag{6.4}$$

which can be written as the following

$$\sum_i \sum_j ln\frac{P(i,j)}{Q(i,j)}(P(i,j) - Q(i,j)) = \sum_i \sum_j ln\frac{Q(i,j)}{P(i,j)}(Q(i,j) - P(i,j)) \tag{6.5}$$

One problem occurs when either $P(i,j)$ or $Q(i,j)$ is zero, which result in an infinite divergence. One possible solution is to add a small value ϵ to the whole distribution. This will not give an exact measure on the data, but it gives some kind of indication on similarities between distribution. The problem still lies on how we choose our ϵ, since a small value would highly affect the logarithmic term. In the following examples, 40 distances from different 2D histograms have been calculated. In these distances, the effect of ϵ has been studied, by choosing the following $\epsilon = 10^{-3}$. From there the ratio between the distances have been calculated, which results in Figure 6.4. From this Figure, the cars show a relative high distance between histograms. The rotor blades show more periodicity, but slightly lower distances, which implies more stability.

6.1.3. PROPOSED ALGORITHM ON REAL DATA

As the rotor blades are more stable in polarization, the proposed algorithm in section 3.2.4 can be used to find differences between vehicles and rotor blades. In this case, a higher correlation coefficient ρ is expected for the rotor blades. In order to classify the targets, the data is averaged, which is done in the following way.

$$\rho_{i,j}(k,l) = \frac{\frac{1}{4NM}\sum_{m=l-M}^{l+M}\sum_{n=k-N}^{k+N}(S_i(m,n) * S_j(m,n))}{\frac{1}{4NM}\sum_{m=l-M}^{l+M}\sum_{n=k-N}^{k+N}S_i(m,n)) * \frac{1}{4MN}\sum_{m=l-M}^{l+M}\sum_{n=k-N}^{k+N}S_j(m,n)} \tag{6.6}$$

where i and j can be either S_{HH}, S_{HV} or S_{VV}. For Time-Range domain: $N = 10$ (Doppler domain), $M = 30$ (range domain). A lower value for N is chosen, because the S_{HH} and S_{VV} highly vary in intensity in Doppler domain, as seen in Figure 6.1. The ρ has been computed for a series of time intervals of 512 (approximately 0.5 s) time samples

The ρ of the blade highly depends on its orientation and the reflected part of the blade. In general, the values are either low or quite high, which can be seen in Figure 6.5(f). The ρ values of the cars are in general lower as seen in Figure 6.5(a). To verify this phenomenon, histograms of the correlation coefficient for both vehicles and wind turbines are shown in Figure 6.6 and 6.7. To further extend this approach, the spectrogram is shown in Figure 6.8.

Unfortunately, this highly depends on the vehicle as ρ values can be similar to the ρ of the wind turbine. Though, there are a lot of cases where the vehicle can be seperated from the wind turbine blades.

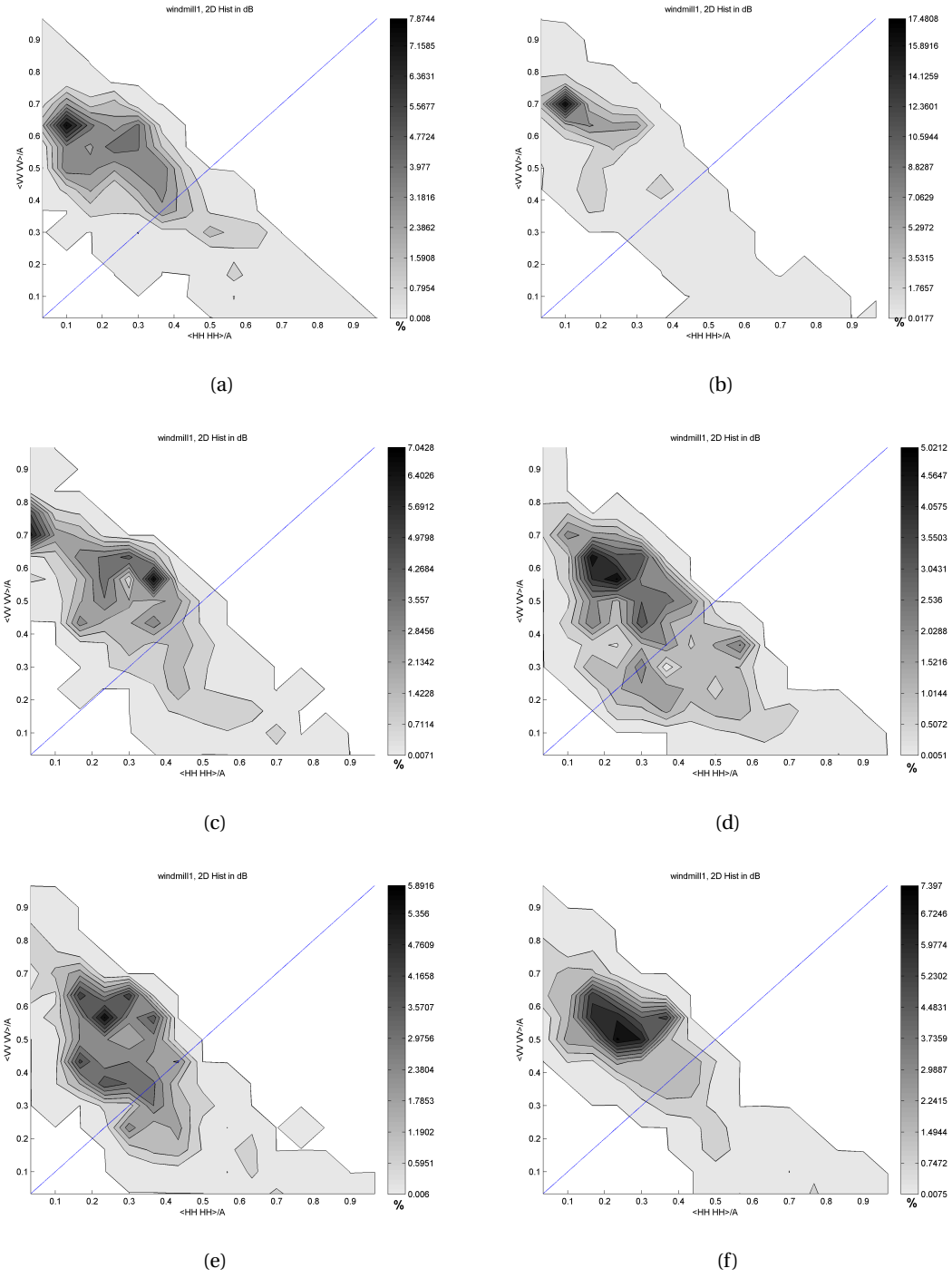

Figure 6.2: Two dimensional histogram of blades in six consecutive time frames

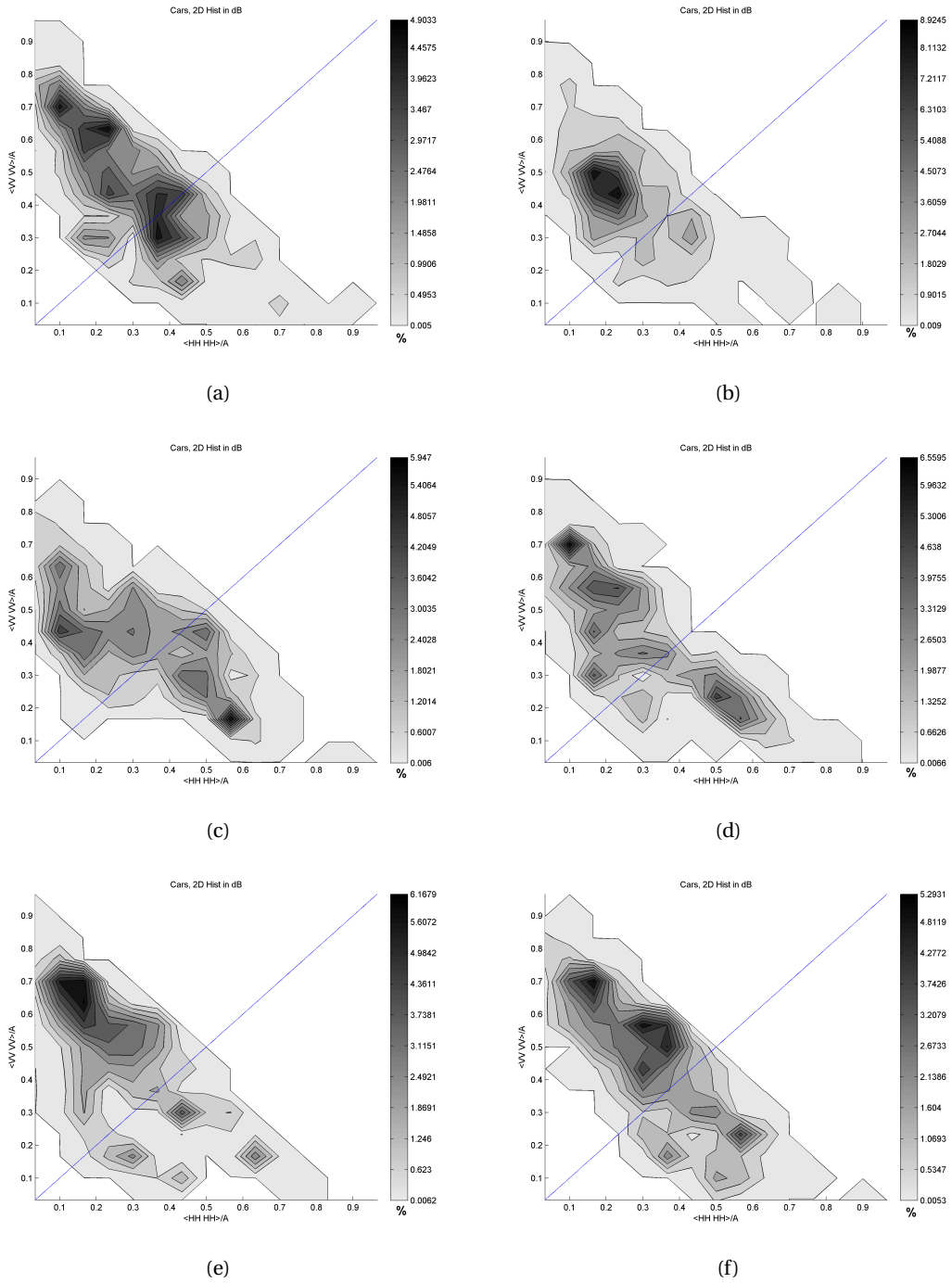

Figure 6.3: Two dimensional histogram of vehicles in six consecutive time frames

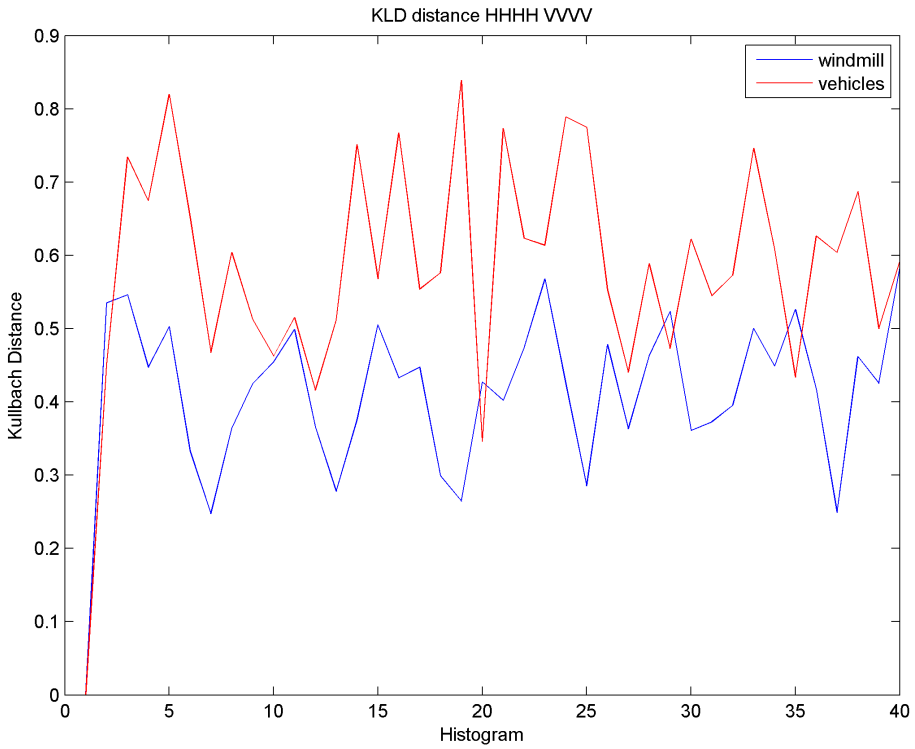

Figure 6.4: Kullback-Leibler Distance for vehicles and rotor blades

6.2. DIRECT ESTIMATION OF POLARIZATION INVARIANTS

This section describes the Huynen parameters which can be directly estimated by using certain algorithms described in [12] on the scattering matrix. This principle can be explained in the following way. Assuming a linear basis, the scattering matrix described in section 2.2.1 can be written as the following

$$S = T^T * E^T * S_e * E * T * e^{j\phi} = \begin{bmatrix} \dot{S}_{HH} & \dot{S}_{HV} \\ \dot{S}_{HV} & \dot{S}_{HV} \end{bmatrix} \tag{6.7}$$

where

$$S_e = \begin{bmatrix} \dot{\lambda_1} & 0 \\ 0 & \dot{\lambda_2} \end{bmatrix} = m * e^{j\phi} * \begin{bmatrix} e^{j\nu} & 0 \\ 0 & e^{-j\nu} \end{bmatrix} \begin{bmatrix} 1 & 0 \\ 0 & tan^2\gamma \end{bmatrix} \begin{bmatrix} e^{j\nu} & 0 \\ 0 & e^{-j\nu} \end{bmatrix} \tag{6.8}$$

is the scattering matrix of the target in the eigenpolarization basis, where $\dot{\lambda_1}$ and $\dot{\lambda_2}$ are complex eigenvalues of the scattering matrix. These eigenvalues take the following form

$$\dot{\lambda}_1 = m * e^j 2\nu + \phi \qquad \dot{\lambda}_2 = m * tan^2\gamma e^j 2\nu + \phi \tag{6.9}$$

Transformation matrices T and E can be written as the following rotation matrices.

$$T = \begin{bmatrix} \cos(\theta) & \sin(\theta) \\ \sin(\theta) & \cos(\theta) \end{bmatrix} \tag{6.10}$$

$$E = \begin{bmatrix} \cos(\epsilon) & j\sin(\epsilon) \\ j\sin(\epsilon) & \cos(\epsilon) \end{bmatrix} \tag{6.11}$$

The scattering parameters can be described with the help of Huynen-Euler (m, θ, ϵ, ν and γ) parameters [13], which are related to the physical characteristics of the target [12].

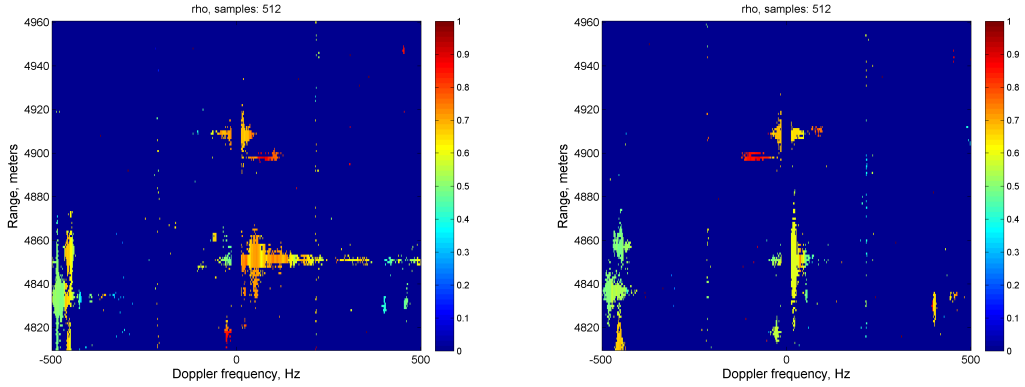

(a)

(b)

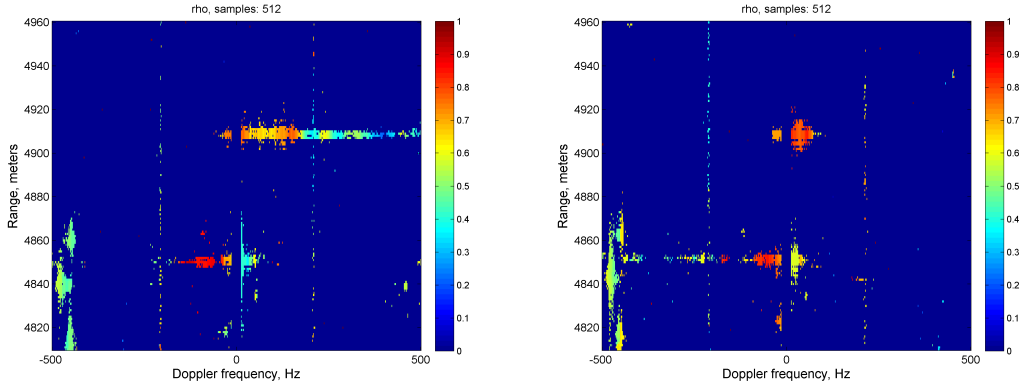

(c)

(d)

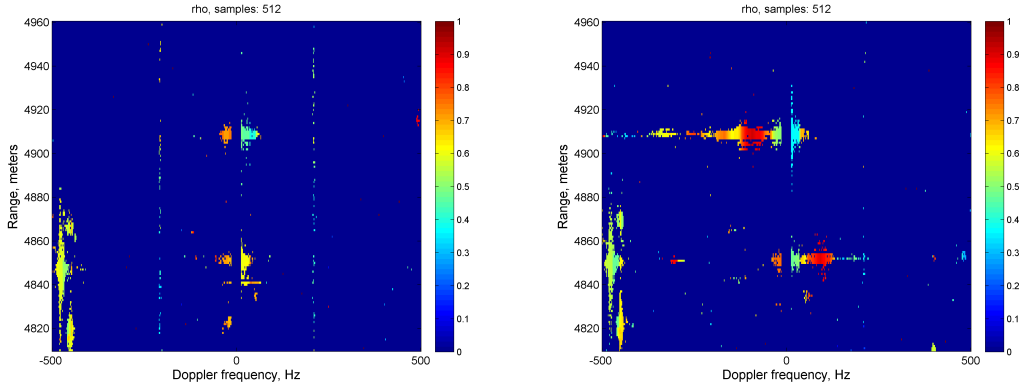

(e)

(f)

Figure 6.5: ρ with 512 frequency samples

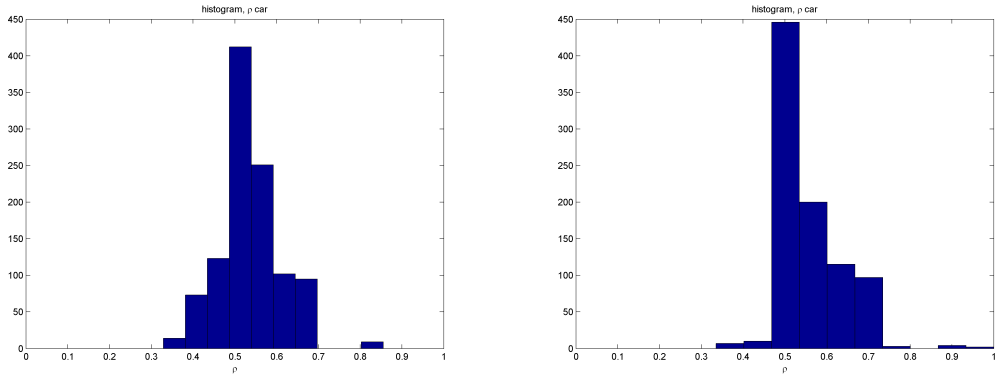

(a)

(b)

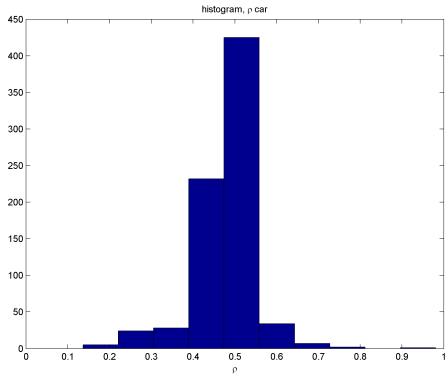

(c)

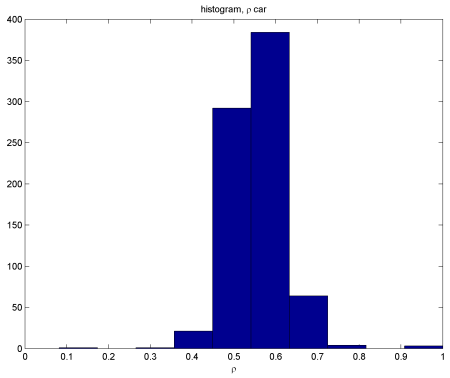

(d)

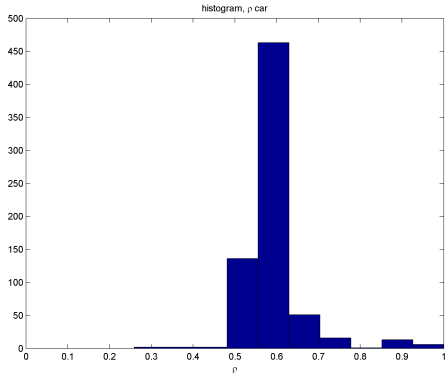

(e)

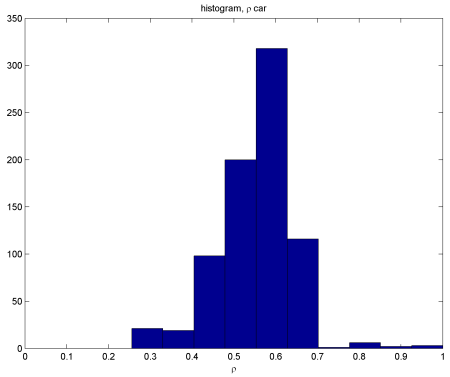

(f)

Figure 6.6: ρ histogram of the vehicles with 512 frequency samples

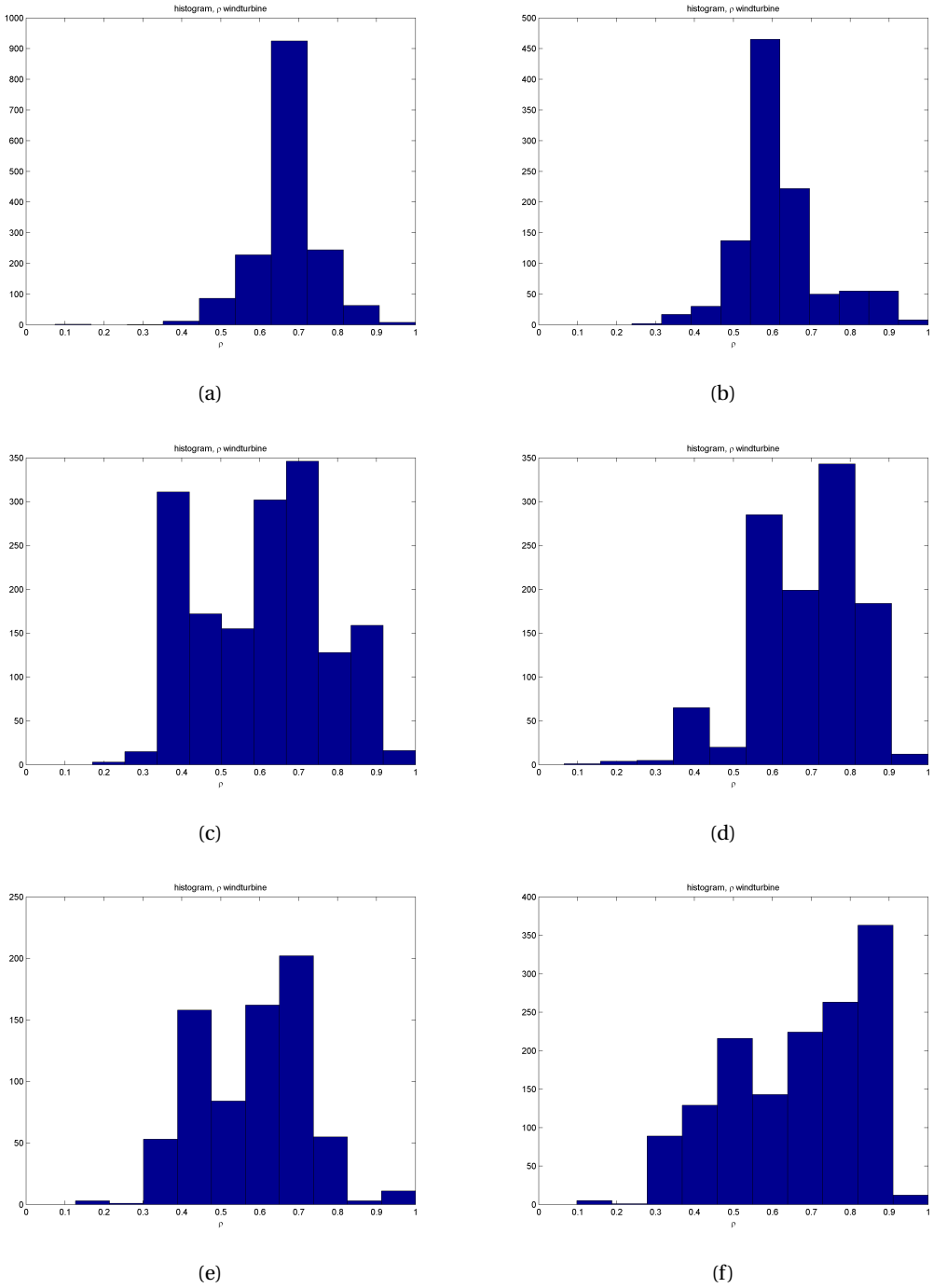

(a) (b)

(c) (d)

(e) (f)

Figure 6.7: ρ histpgrams of the cars with 512 frequency samples

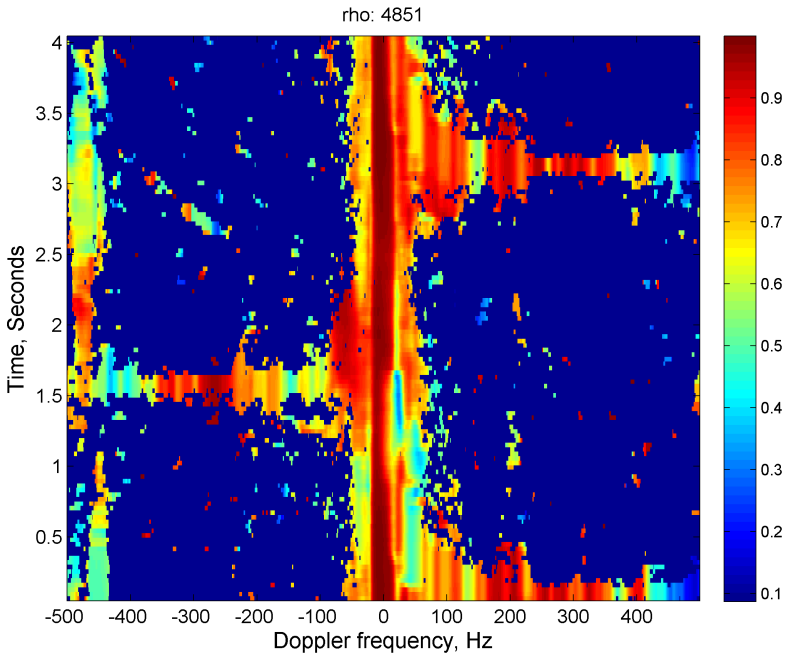

Figure 6.8: Correlation coefficient

- m: Maximum radar cross section of the target. The maximum cross radar of the target in Figure 6.9 shows stronger reflections from the tower, vehicles and the slower parts of the blade. As the rotor blades have relative weaker reflections, there is some potential to mitigate that target.

- ϕ: Orientation angle related to the target orientation around the line of sight. The orientation angle in Figure 6.10 shows some differences between vehicles and wind turbine. The orientation angle of the vehicles are rather stable. As a large part of the turbine show different values, there is a lot potential in suppressing the turbine.

- τ: Ellipticity angle related to the symmetry of the target. ($\tau = 0$ for man-made structures, $\tau = \frac{\pi}{4}$ for natural media). The ellipticity angle shown in Figure 6.11 is close to 0 for both vehicles and wind turbine. As both are man-made structures, this is very reasonable. Though, some parts show higher values as these parts are less smooth.

- ν: Skip angle, related to multi-bouncing ($\nu = 0$ for single bouncing, $\nu = \frac{\pi}{4}$ for double bouncing). The skip angle shown in Figure 6.12 is small for the tower and vary for the vehicles and rotor blades. This could be reasonable as double bouncing is more common on vehicles and blades. Due to the high dependence on phase, this parameter is questionable.

- γ: Polarizability angle ($\gamma = 0$ for dipole, $\gamma = \frac{\pi}{4}$ for a surface or sphere). The polarizability angle in Figure 6.13 is quite high for all targets, which implies that the targets are similar to a sphere, dihedral or surface. Therefore, the thick dipole model could be inaccurate.

These parameters depend on the real and imaginary values of the elements of the scattering matrices, which are obtained by the algorithms in [12]. Unfortunately, these parameters depend on the phase which is affected by the residual phase and result in biased results.

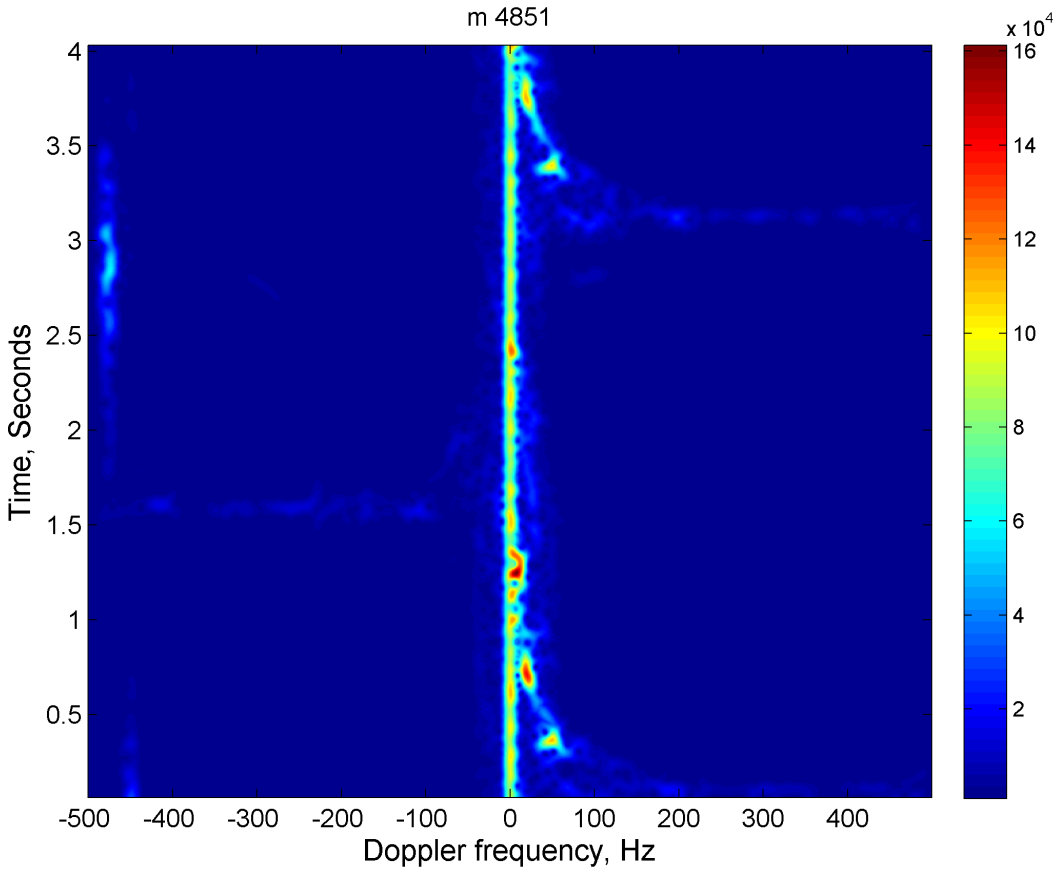

Figure 6.9: Radar Cross Section

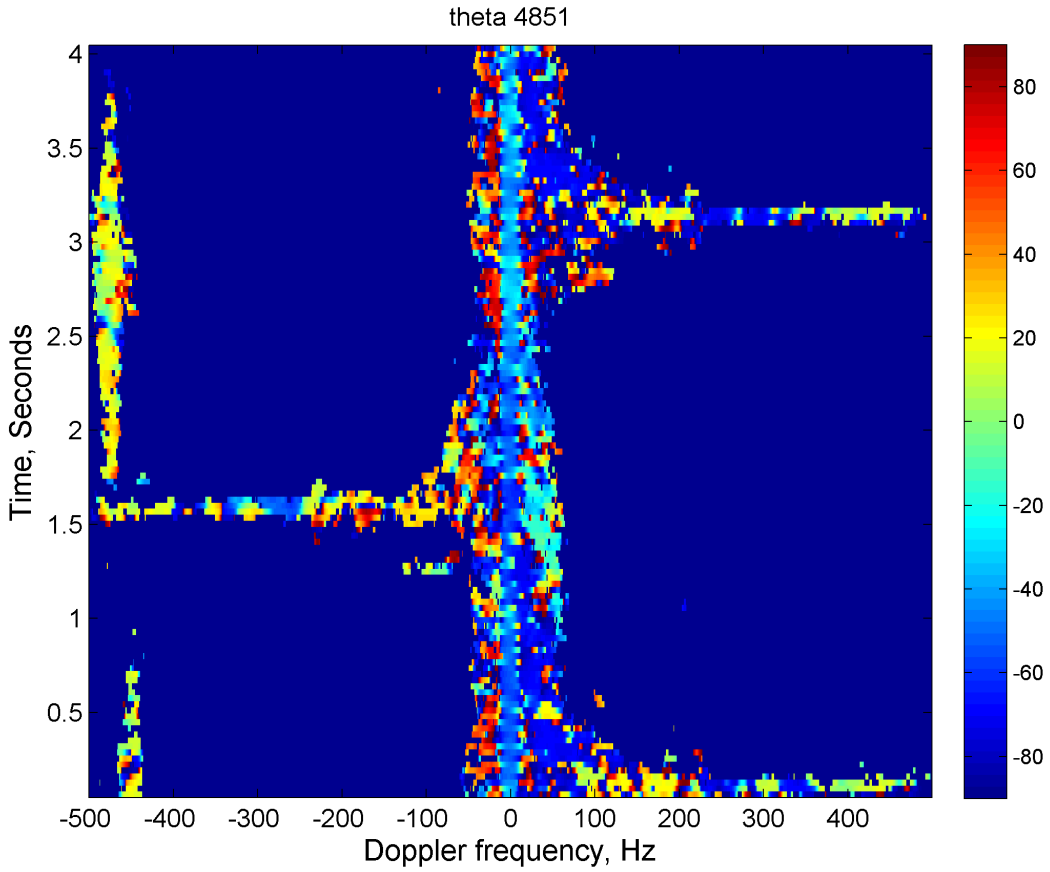

Figure 6.10: Orientation angle

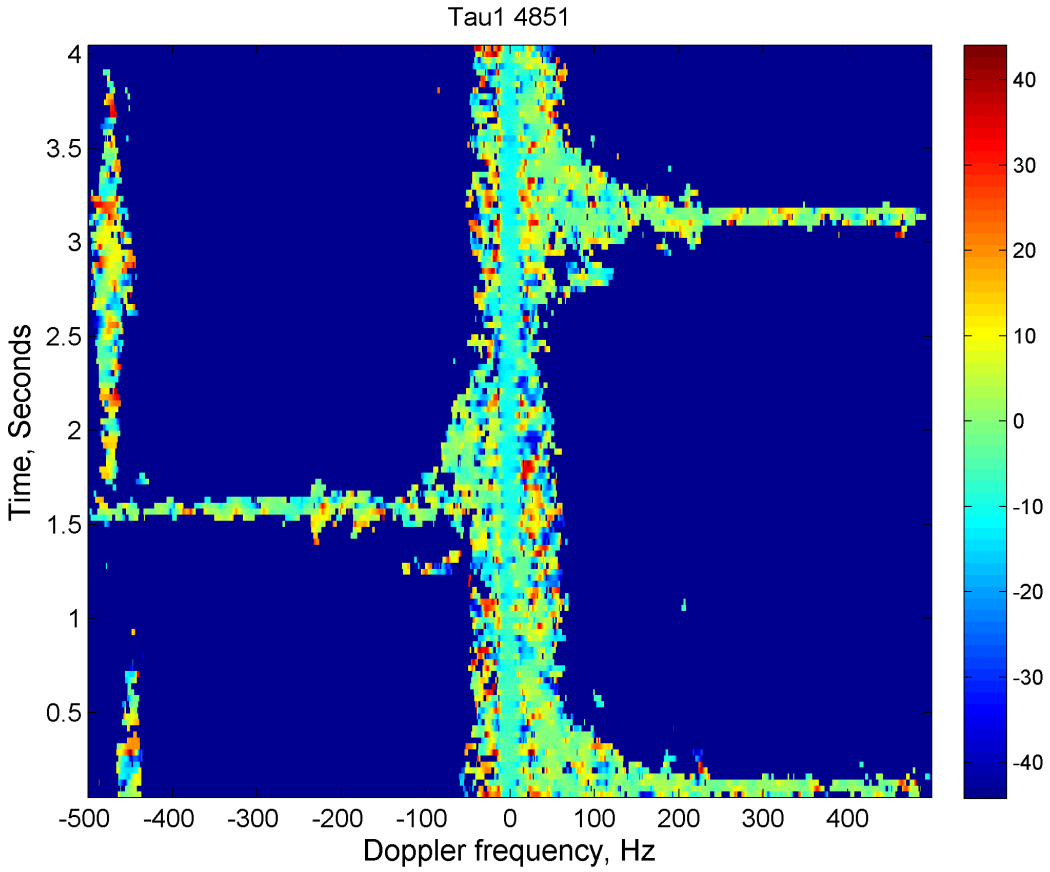

Figure 6.11: Ellipticity angle

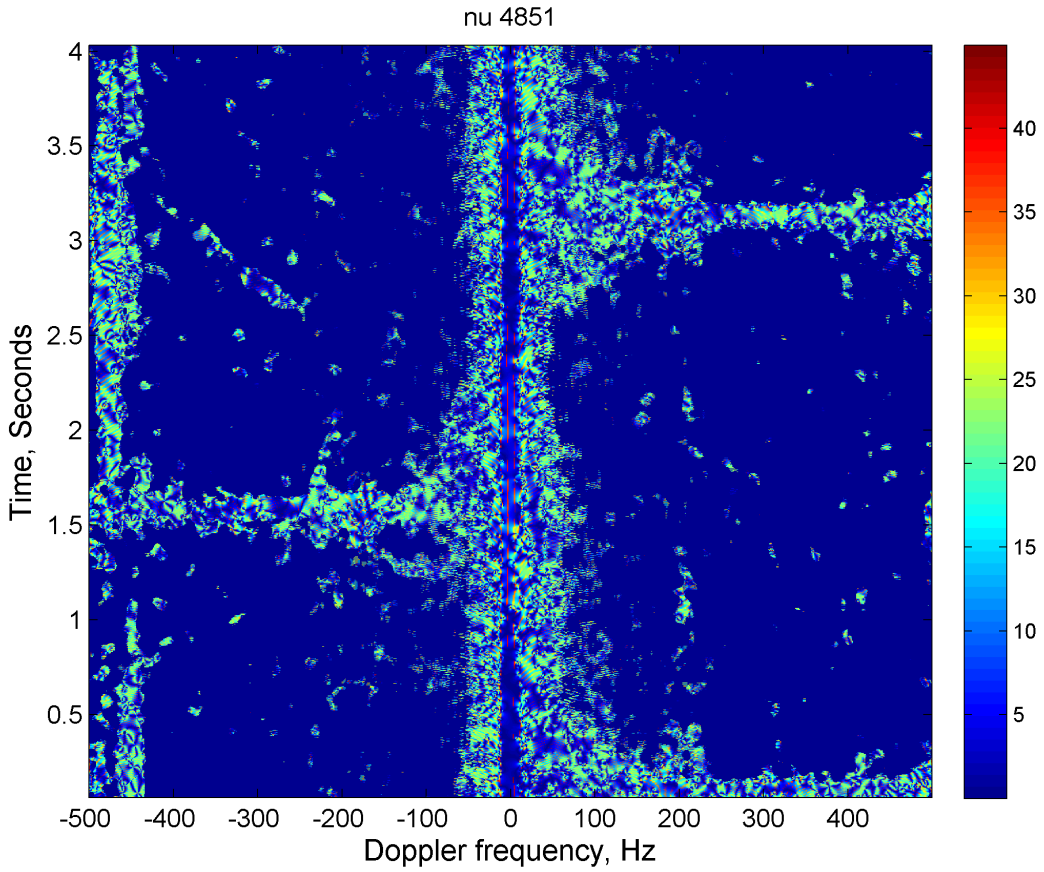

Figure 6.12: Skip angle

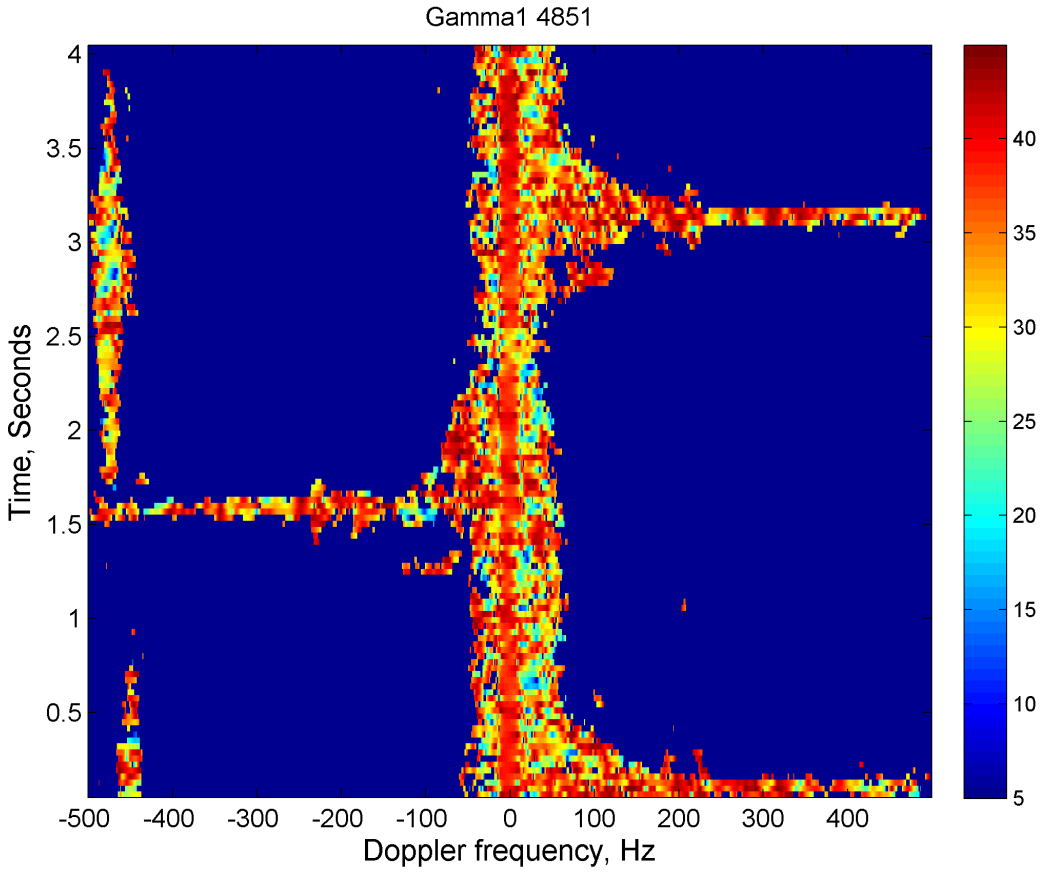

Figure 6.13: Polarizability angle

6.3. DECOMPOSITION THEOREM

Target decomposition theorem helps to determine the (dominant) scattering mechanism, by expressing the scattering matrix as a combination of independent scattering matrices which are related to a specific scattering mechanism. For each target, it is possible to gain knowledge on the characterization and it may be useful to distinguish one target from another. Huynen was the first person who formalized target decomposition.

6.3.1. PAULI DECOMPOSITION

Pauli decomposition is based on coherent decomposition which assumes that the scattering matrix can be written as a combination of basis matrices. This decomposition expresses the scattering matrix into a combination of the following Pauli matrices.

$$S = \begin{bmatrix} S_{HH} & S_{HV} \\ S_{VH} & S_{VV} \end{bmatrix} = a \begin{bmatrix} 1 & 0 \\ 0 & 1 \end{bmatrix} = b \begin{bmatrix} 1 & 0 \\ 0 & -1 \end{bmatrix} = c \begin{bmatrix} 0 & 1 \\ 1 & 0 \end{bmatrix} = d \begin{bmatrix} 0 & -j \\ j & 0 \end{bmatrix} \tag{6.12}$$

where a, b, c and d are all complex parameters given by

$$a = \frac{S_{HH} + S_{VV}}{\sqrt{2}} \tag{6.13a}$$

$$b = \frac{S_{HH} - S_{VV}}{\sqrt{2}} \tag{6.13b}$$

$$c = \frac{S_{HV} + S_{VH}}{\sqrt{2}} \tag{6.13c}$$

$$d = j\frac{S_{HV} - S_{VH}}{\sqrt{2}} \tag{6.13d}$$

The Pauli decomposition is illustrated in Figure 6.14 to 6.16, where the three a, b and c are represented as spectrograms. Note that these values are normalized for comparison purposes.

- a: Represents single scattering from a plane surface. This is shown in Figure 6.14, where $|a|^2$ is stronger at the smooth parts of the wind turbine. The tower ($F_D = 0$) and large parts of the rotor blade are clearly dominant. This implies that the blade behaves more as a surface than a dipole. For vehicles, this parameter is weaker, but still clearly visible.
- b: Describes dihedral scattering with a orientation of 0^o. This is shown in Figure 6.15, where $|b|^2$ is stronger for dihedral scatterers of the wind turbine. The stronger parts are found at 1.5s on the lower positive Doppler frequency, which is the result of double scattering between blade and tower.
- c: Describes dihedral scattering with a orientation of 0^o. It is often associated with volume scattering. This is illustrated in Figure 6.16, where $|c|^2$ stands for volume scattering. This parameter more visible on cars and on the lower Doppler frequencies corresponding to the movement of the blade.
- d: Presents the antisymmetric components of the scattering matrix. In the monostatic case, this parameter should be 0. However, there seems to be some calibration problem between S_{HV} and S_{VH} which is seen in section 5.3.3. Still, this parameter is barely visible on the spectrogram and can be neglected.

In general, the Pauli decomposition shows some differences between vehicle and wind turbine. The vehicle is a mixture between parameter a, b and c, while the majority of the wind turbine is dominated by parameter a. Again, these results are affected by the residual phase. Still there is some definite potential in decomposition algorithms to classify certain targets. Therefore, $H/\overline{\alpha}$ decomposition is studied in the next section.

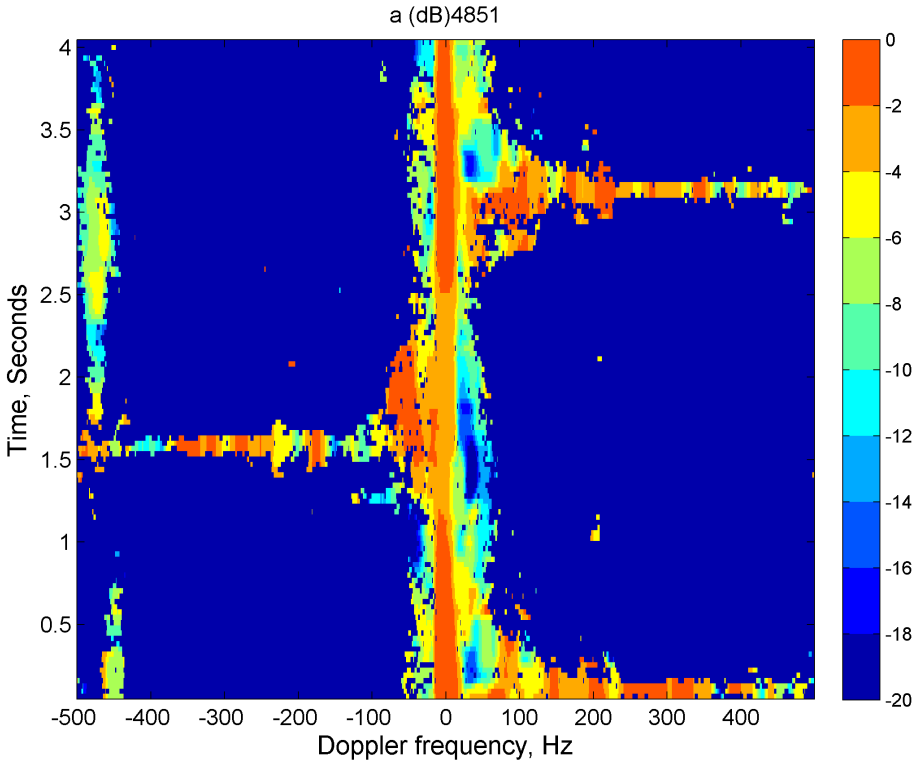

Figure 6.14: $|a|^2$

6.3.2. $H/\overline{\alpha}$ DECOMPOSITION

Another decomposition theorem is the $H/\overline{\alpha}$ decomposition theorem. This theorem is based on the eigenvector/eigenvalue analysis of the coherency matrix T, which provides a basis invariant description of the scatterer [14]. Eigenvector analysis provides information about the different types of scattering processes, while eigenvalue analysis gives information on their relative magnitude. The coherency matrix is a function of the Pauli vector $\vec{k}$ and can be written as

$$T = < \vec{k}\vec{k}^{*T} > \tag{6.14}$$

where the Pauli vector can be written as

$$\vec{k} = \frac{1}{\sqrt{2}} = \begin{bmatrix} S_{HH} + S_{VV} & S_{HH} - S_{VV} & 2S_{XY} \end{bmatrix} \tag{6.15}$$

The 3 x 3 coherency matrix obtained from equation 6.14 can be written in the following form.

$$T = U_3 \Sigma U_3^- 1 \tag{6.16}$$

where Σ is a 3 x 3 diagonal matrix with eigenvalues of the T matrix as seen in the following

$$\Sigma = \begin{bmatrix} \lambda_1 & 0 & 0 \\ 0 & \lambda_2 & 0 \\ 0 & 0 & \lambda_3 \end{bmatrix} \tag{6.17}$$

$U_3 = [\vec{u}_1 \vec{u}_2 \vec{u}_3]$ is a 3 x 3 unitary matrix, where $\vec{u}_1, \vec{u}_2 and \vec{u}_3$ stand for the three unit orthogonal eigen vectors. The T matrix, as seen in, can be described as a summation of three independent targets,

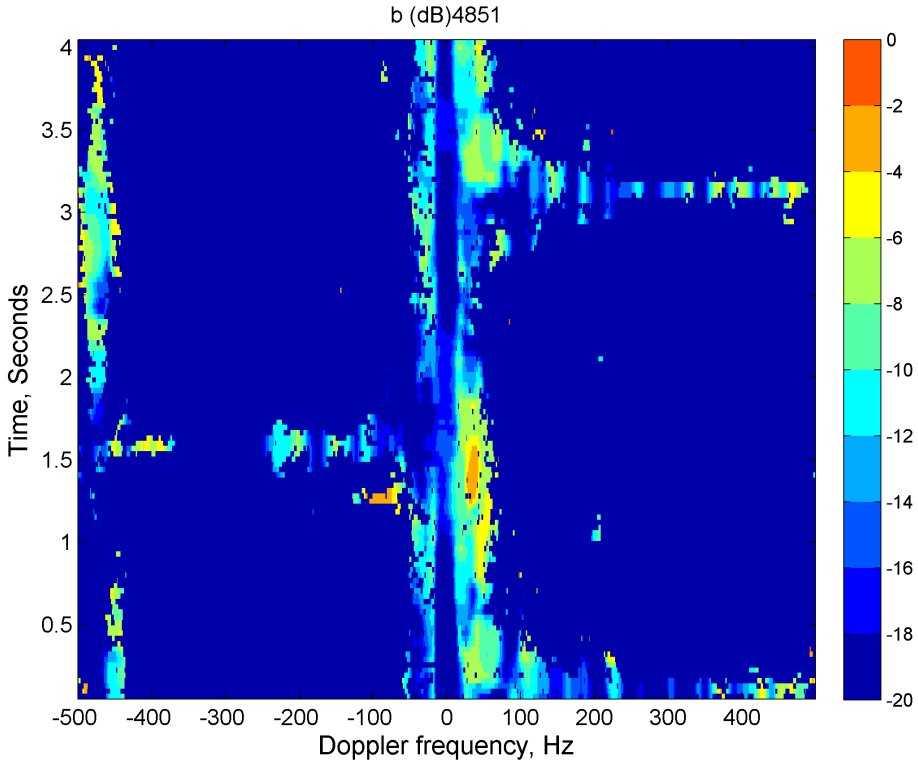

Figure 6.15: $|b|^2$

where each target is represented by a single scattering matrix. This decomposition can be written as the following

$$T = \sum_{i=1}^{i=3} \lambda_i T_i = \sum_{i=1}^{i=3} \lambda_i \vec{\boldsymbol{u}}_{\boldsymbol{i}} * \vec{\boldsymbol{u}}_{\boldsymbol{i}}{}^{T*} \tag{6.18}$$

6.3.3. PROBABILISTIC MODEL FOR RANDOM MEDIA SCATTERING

A parametrization of the eigenvectors of the averaged coherency T matrix takes the following form

$$\vec{\boldsymbol{u}} = [\cos\alpha e^{j\phi} \quad \sin\alpha\cos\beta e^{j\delta+\phi} \quad \sin\alpha\sin\beta e^{j\gamma+\phi}]^T \tag{6.19}$$

which gives the following matrix 3 x 3 matrix, considering $U_3 = \left[\vec{\boldsymbol{u}}_{\boldsymbol{1}}\vec{\boldsymbol{u}}_{\boldsymbol{2}}\vec{\boldsymbol{u}}_{\boldsymbol{3}}\right]$

$$U_3 = \begin{bmatrix} \cos\alpha_1 e^{j\phi_1} & \cos\alpha_2 e^{j\phi_2} & \cos\alpha_3 e^{j\phi_3} \\ \sin\alpha_1\cos\beta_1 e^{j\delta_1+\phi_1} & \sin\alpha_2\cos\beta_2 e^{j\delta_2+\phi_2} & \sin\alpha_3\cos\beta_3 e^{j\delta_3+\phi_3} \\ \sin\alpha_1\sin\beta_1 e^{j\gamma_1+\phi_1} & \sin\alpha_2\sin\beta_2 e^{j\gamma_2+\phi_2} & \sin\alpha_3\sin\beta_3 e^{j\gamma_3+\phi_3} \end{bmatrix} \tag{6.20}$$

The target is modeled as the sum of the three columns of the 3 x 3 unitary U_3 matrix, where the amount of occurrences is based on the pseudo-probabilities P_i given by

$$P_i = \frac{\lambda_i}{\sum_{k=1}^{3} \lambda_k} \tag{6.21}$$

As an example, consider the target parameter x, with the following random sequence

$$x = [x_1 x_2 x_2 x_3 x_1 x_3 x_2 ...] \tag{6.22}$$

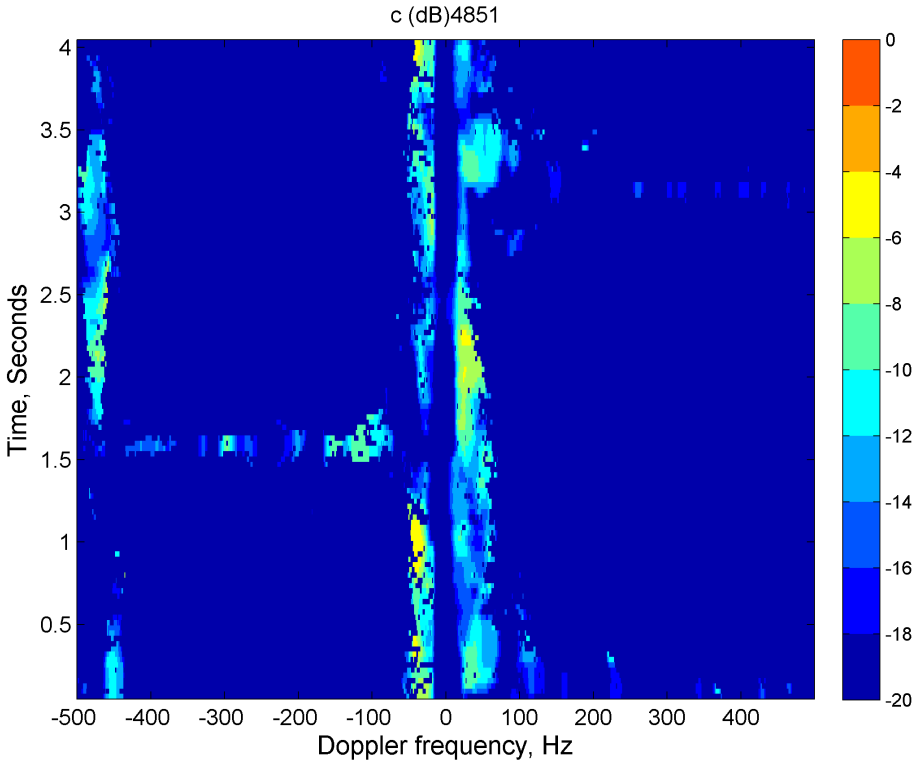

Figure 6.16: $|c|^2$

where the best estimate of parameter x is given by the mean of the sequence.

$$\overline{x} = \sum_{k=1}^{3} P_k x_k \tag{6.23}$$

Using the mean parameters of the dominant scattering matrix can be extracted from the 3 x 3 coherency matrix. This will lead to a mean unit target vector $\vec{\boldsymbol{u}}_{\mathbf{0}}$, which can be constructed as

$$\vec{\boldsymbol{u}}_{\mathbf{0}} = e^{j\phi} = \begin{bmatrix} \cos\overline{\alpha} \\ \sin\overline{\alpha}\cos\overline{\beta}e^{j\overline{\delta}} \\ \sin\overline{\alpha}\sin\overline{\beta}e^{j\overline{\gamma}} \end{bmatrix} \tag{6.24}$$

From the unit vector $\vec{\boldsymbol{u}}_{\mathbf{0}}$, it is possible to obtain the mean target vector $\vec{\boldsymbol{k}}_{\mathbf{0}}$, which corresponds to the following.

$$\vec{\boldsymbol{k}}_{\mathbf{0}} = \overline{\lambda}e^{j\phi} = \begin{bmatrix} \cos\overline{\alpha} \\ \sin\overline{\alpha}\cos\overline{\beta}e^{j\overline{\delta}} \\ \sin\overline{\alpha}\sin\overline{\beta}e^{j\overline{\gamma}} \end{bmatrix} \tag{6.25}$$

where the parameter $\overline{\lambda}$ stands for the mean target power, which is defined by

$$\overline{\lambda} = \sum_{k=1}^{3} P_k \lambda_k \tag{6.26}$$

6.3.4. POLARIMETRIC SCATTERING $\overline{\alpha}$ PARAMETER

The identification of the type of scattering is mostly done by the interpretation parameter $\overline{\alpha}$, which can be obtained from equation 6.25. Its value can be easily related to the physics behind the scat-

tering process. The value of $\overline{\alpha}$ can range between 0 to 90^o, where each value between that range corresponds to a specific scattering mechanism. The following cases can be considered.

- $0 \leq \overline{\alpha} \leq 42.5^o$: represents odd bounce surface scattering in geometrical optics ($\alpha = 0$) to odd bounce surface scattering under physical optics to the Bragg surface model ($0 < \alpha \geq 42.5^o$).
- $42.5^o < \overline{\alpha} < 47.5^o$: represents dipole scattering or single scattering by a cloud of anisotropic particles.
- $47.5^o \leq \overline{\alpha} \leq 90^o$: represents double bounce scattering between two dielectric surfaces ($47.5^o \leq \overline{\alpha} < 90^o$) to dihedral scattering from metallic surfaces ($\overline{\alpha} = 90^o$)

6.3.5. POLARIMETRIC SCATTERING ENTROPY (H)

Parameter H is the entropy and highly depends on the eigenvalues of the T matrix. If only one eigenvalue is nonzero, then the statistical weight reduces to a point-scattering Sinclair matrix. In the other extreme where all eigenvalues are identical, the average coherency T matrix represents a completely de-correlated random scattering structure. Between these extremes, the T matrix represents a depolarized structure of scatterers. In order to find the degree of statistical disorder of each different scattering mechanism in the scattering structure, the polarimetric scattering entropy is used and defined by the eigenvalues in the following way

$$H = -\sum_{k=1}^{N} P_k log_N(P_k) \tag{6.27}$$

where P_i refers to the pseudo probabilities obtained from the eigenvalues. N is equal to the dimension of the coherency matrix ($N = 3$ in the monostatic case and $N = 4$ in the bistatic case). For different values of $H (0 < H < 1)$, the following cases can be distinguished.

- $H = 0$: represents a single scattering mechanism. Only one eigenvalue is nonzero.
- $H < 0.3$: represents a weakly depolarizing system and the dominant scattering mechanism is identifiable.
- $H > 0.3$: represents a depolarized system. A mixture of possible point scatterer types must be considered.
- $H = 1$: represents a completely depolarized system and behaves as a truly random noise process.

6.3.6. $H/\overline{\alpha}$ CLASSIFICATION SPACE

The entropy and mean $\overline{\alpha}$ images of the wind turbine are seen in spectrograms 6.17(a) and 6.17(b). In order to average, equation 6.28 has been used

$$< T_{i,j}(k,l) >= \frac{1}{4NM} \sum_{n=k-N}^{k+N} \sum_{m=l-M}^{l+M} (T_{i,j}(n,m)) \tag{6.28}$$

where i and j define the specific element of the coherency matrix. N defines the Doppler space and M the time space, where both $N = M = 3$. To interpret the values, Cloude and Pottier proposed a classification scheme based on the use of a two dimensional $H/\overline{\alpha}$ plane in [14]. This plane is divided into 9 zones that each correspond to a specific scattering characteristics as shown in Figure 6.18.

- Zone 9 is characterized by a low entropy surface scatterer with $\overline{\alpha}$ values less than 42.5. This implies surface scattering where Bragg surface scattering is included in this zone.

- Zone 8 is interpreted by a low entropy dipole scattering. This zone shows a large imbalance between S_{HH} and S_{VV} in amplitude. Isolated dipole scatterers would appear in this zone. According to our hypothetical model, the majority of the scatterers would fall in this category.
- Zone 7 represents low entropy with multiple scattering events. This zone corresponds to low entropy with double, or even bounce scattering due to the isolated dielectric and metallic dihedral scatterers.
- Zone 6 corresponds to a medium entropy surface scatterer. The medium entropy is caused by a change in roughness of a surface. Also note that the minimum mean alpha increases with the entropy. This is the consequence of a higher randomness, which most likely eliminates the possibility of a low mean alpha.
- Zone 5 is medium entropy vegetation scattering. This zone includes moderate entropy with a dominant dipole scattering mechanism. One example could be scattering from tree branches from a tree, where the entropy is higher due to the distribution of orientation angles.
- Zone 4 represents medium entropy and includes multiple scattering, such as dihedral and double bounce scattering. In general, dense urban areas fall into this category.
- Zone 3 shows High entropy with surface scattering. It's a non-feasible area and due to the high entropy it is likely not able to classify this as surface scattering.
- Zone 2 is shown as a high entropy vegetation scatterer. In general, scattering from forest canopies could lie in this category. Extreme behavior in this class is most likely linked with noise.
- Zone 1 is classified as high entropy multiple scattering. Double or dihedral scattering is still possible to distinguish. This zone can be linked with forest applications with a well-developed branch.

For classification purposes, 2D histograms are obtained of the entropy and $\overline{\alpha}$ of both vehicles and wind turbine. This is shown in Figure 6.19, where different values for H and $\overline{\alpha}$ are observed between vehicles and wind turbine. Unfortunately. the residual phase problem is still present and therefore additional research is recommended for better reliability. Though, this approach still has a lot potential to distinguish the wind turbine from the vehicles as the density of the 2D histograms are found in different places.

6.4. CONCLUSION

This chapter describes the results. Covariance study analyzed the amplitude of the covariance elements for both vehicles and rotor blades. In range Doppler domain it shows little agreement with the established wind turbine model. Still, there were some differences between vehicles and turbines. By applying a correlation coefficient algorithm, values were different for blades and vehicles. However, this highly depends on the vehicle and orientation of the blades. Another method is direct estimation of polarization invariants, which made use of algorithms to obtain Huynen parameters which gives information on the targets. As some parameters give a possible solution, it also depends on the complex parameters of the scattering matrix which is influenced by the residual phase. Decomposition theorems have been used. Pauli decomposition shows that the majority of wind turbine behaves like a surface, while the vehicle is a mixture of surface, dihedral and volume scattering. Finally, the $H/\overline{\alpha}$ decomposition helped categorizing different targets with certain scattering mechanisms. Even though there were some clear differences between vehicles and blades, the results are still affected by the residual phase. For better reliability of these results, additional analysis on the residual phase problem is recommended.

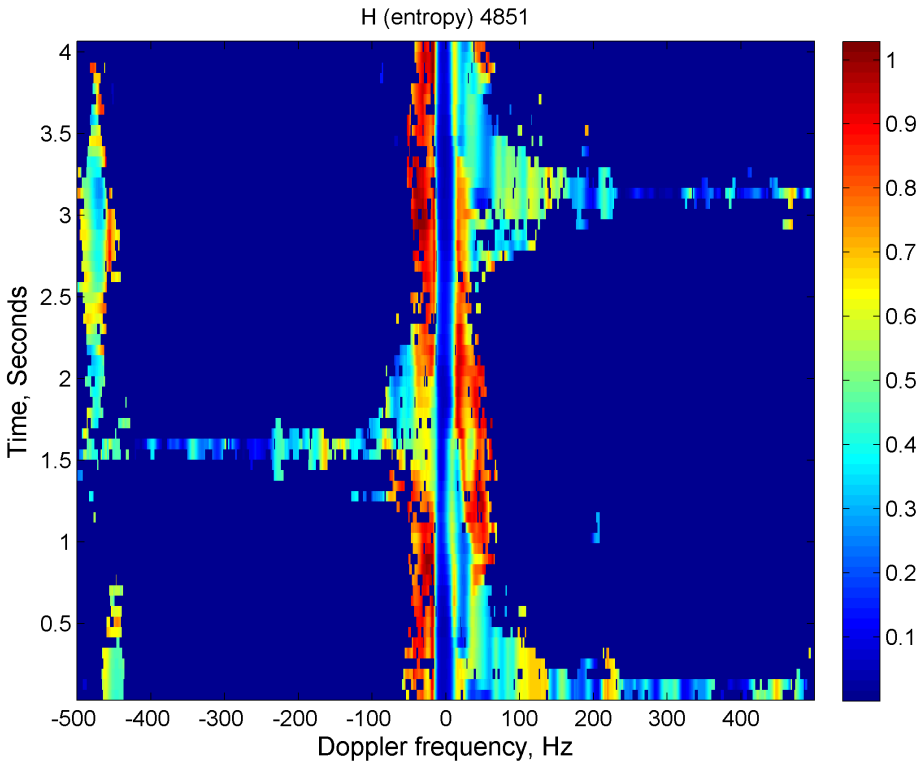

(a) Entropy

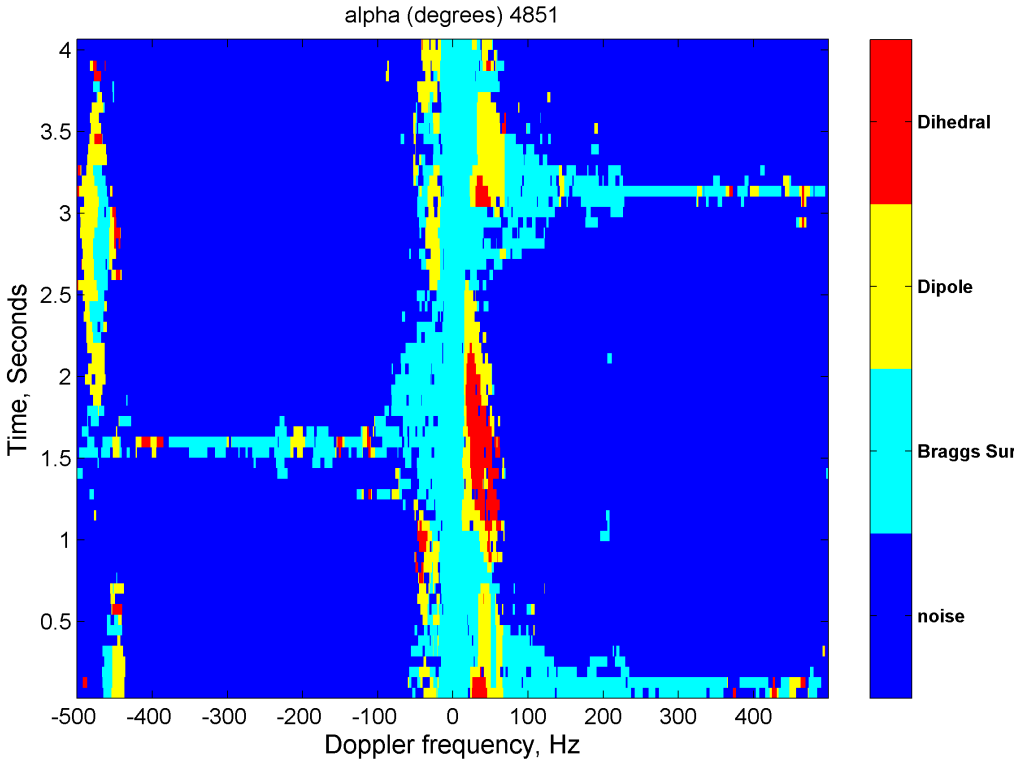

(b) $\overline{\alpha}$

Figure 6.17: H and $\overline{\alpha}$

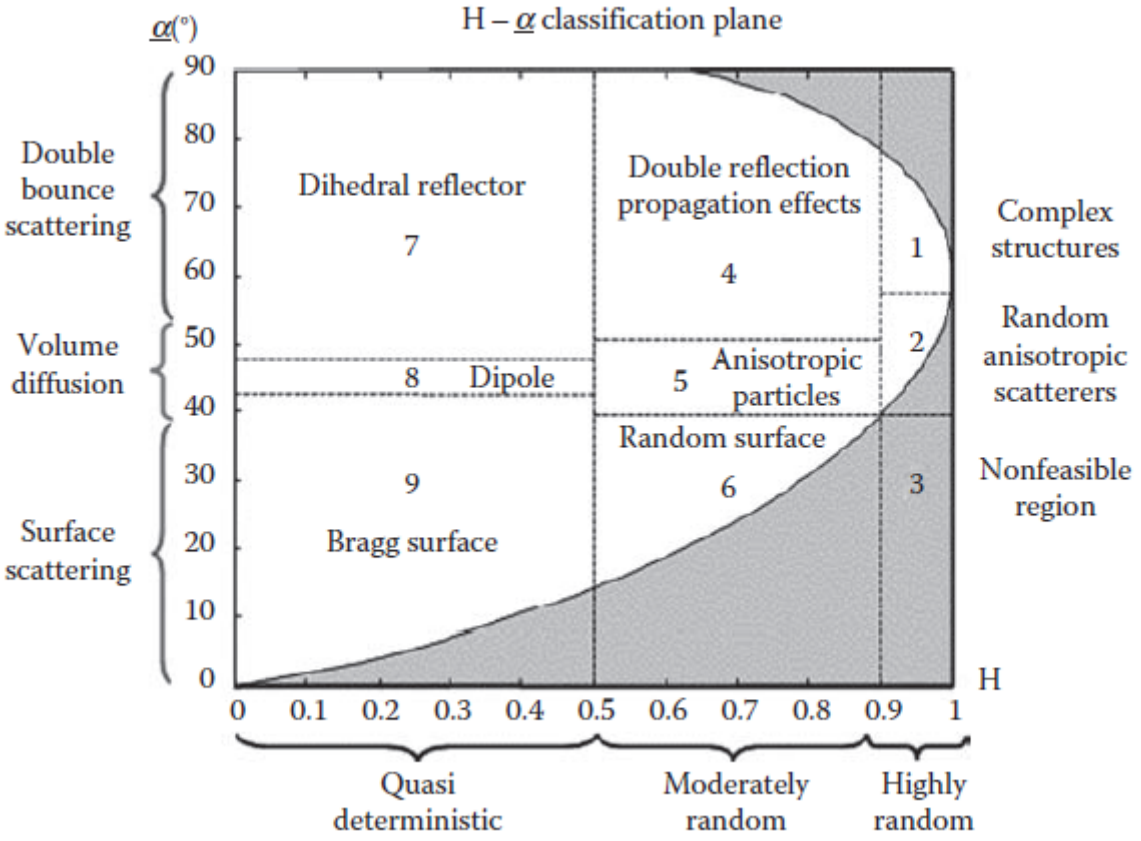

Figure 6.18: Two-dimensional $H/\overline{\alpha}$

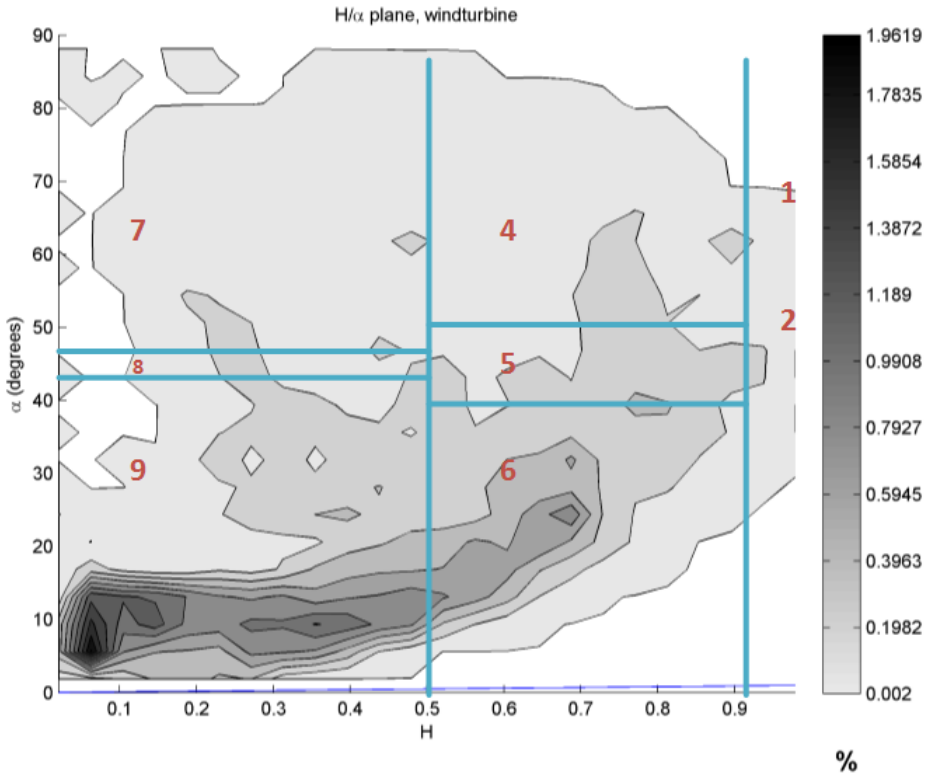

(a) Wind turbine

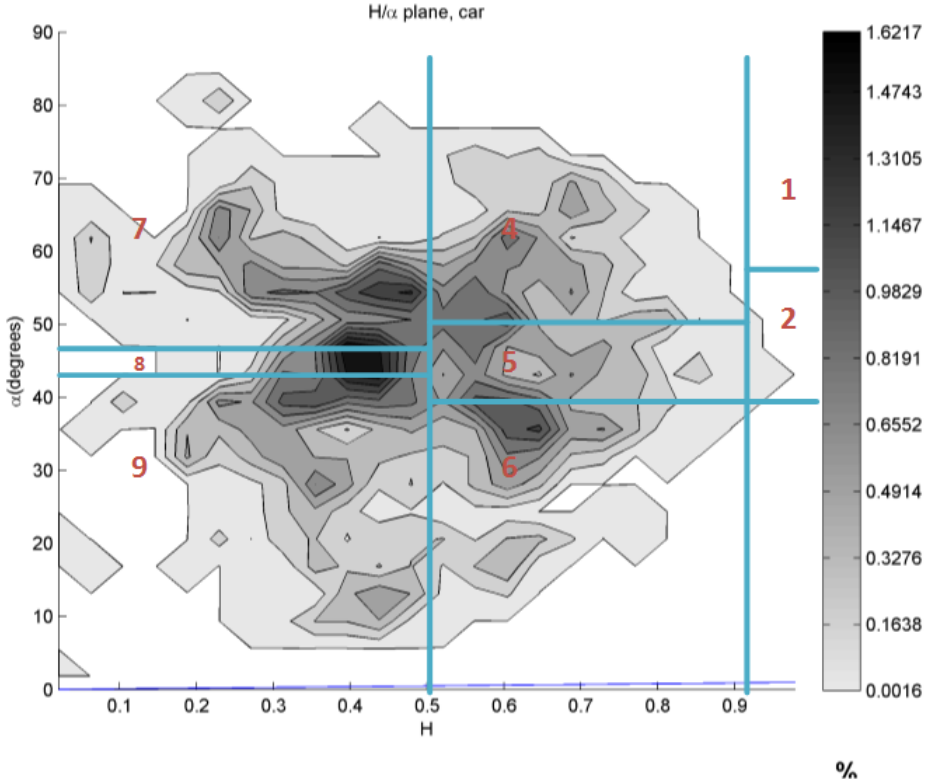

(b) Cars

Figure 6.19: H - $\overline{\alpha}$ classification scheme

7

CONCLUSION AND FURTHER RESEARCH

This chapter concludes the thesis and consists in the following way: Section 7.1 draws conclusions from each chapter; section 7.2 provides recommendations for future work.

7.1. CONCLUSION

In this thesis, the effect of wind turbine Doppler clutter has been studied which is mainly caused by the rotating turbine blade. The goal was to find a method to distinguish the Doppler clutter from other moving objects, such as vehicles. Due to the unique and thin design of the blade, polarimetric study has been done to find ways to mitigate the clutter from other objects. In chapter 2, a basic overview has been given on the polarimetric and Doppler theory which serve as basic building blocks for the rest of the thesis.

Chapter 3 gave two theoretical models where a rotating dipole is assumed. The Doppler model is related to the velocity of the dipole and showed the behavior in time and Doppler domain. The polarimetric model showed the effect of amplitude and phase in S_{HH}, S_{HV}, S_{VH} and S_{VV} polarization. Considering a rotating dipole, both models showed great potential in amplitude and phase study.

The measurement set-up is described in chapter 4. The basic principle of the LFM-CW PARSAX radar has been explained as well as the Dual-Orthogonal signal principle. One disadvantage of using dual orthogonal signals is the residual phase, which results in phase shifts which can be positive or negative depending on the polarization.

Data representation of measured data is presented in chapter 5, where two representations are given of a rotating wind turbine. The first representation gives the measured data in Range Doppler domain for a certain time. The second representation gives the Time-Doppler domain of a single range bin. Furthermore, the residual phase problem is explored in more detail regarding the wind turbine scattering.Unfortunately, the residual phase problem could not yet be resolved and more attention will be given on amplitude.

Finally, chapter 6 provided several methods to possibly distinguish the clutter from rotating blade with their results. The first method focuses on amplitude study and used the covariance matrix to compare turbines and vehicles. From the results the amplitude does not agree with the established model which implies that the blade is a more complicated target. As the blade shows more stability in polarization, a correlation coefficient algorithm is applied which showed variable results. This highly depends on the vehicle and the orientation of the blade. The second method was to extract Huynen parameters which is linked to certain characteristics of the target. As these parameters show some potential to distinguish blades with vehicles, it also depends on the phase of the parameters. The third method was by using decomposition theorems to classify the targets. The

$H/\overline{\alpha}$ decomposition theorem definitely shows some definite differences especially in stability. Unfortunately, these decomposition theorems also depend on the phase of the target which is affected by the residual phase.

7.2. FURTHER RESEARCH

Considering the obtained results, there are some several future research recommendations. As the blade was modeled as a thin dipole, the simplistic polarimetric model does not agree with the measurements. Therefore, additional study on the design and polarization characteristics of the blade is recommended in order to get a more accurate model. Another problem is the residual phase problem which reduces the reliability of phase analysis between polarization elements, which is the result of positive and negative phase shifts between these elements. As the theoretical residual phase does not agree with the measured residual phase, the residual phase could not be resolved.

BIBLIOGRAPHY

[1] O. V. Gent, *Toelichting nieuwe radarhinder toetsingsmethode,* (2014).

[2] A. Naqvi, *Investigation of doppler features from wind turbine scattering,* (2010).

[3] J. Jung, U. Lee, S. Kim, and S. Park, *Micro-doppler analysis of korean offshore wind turbine on the l-band radar,* (2013).

[4] M. Robinson, *Multipath-dominant, pulsed doppler analysis of rotating blades,* (2012).

[5] E. P. J.S. Lee, *Polarimetric Radar Imaging From Basics to Applications* (2009).

[6] J. V. Zyl, H. Zebker, and C. Elachi, *Imaging radar polarization signatures,* (1987).

[7] H. Mott, *Antennas for Radar and Communications. A polarimetric Approach* (1992).

[8] O. Krasnov and A. Yarovoy, *Radar micro-doppler of wind-turbines simulation and analysis using rotating linear wired constructions,* (2014).

[9] C. Balanis, *Antenna Theory: Analysis and Design* (2009).

[10] Z. Wang, O. Krasnov, G. Babur, L. Ligthart, and F. V. D. Zwan, *Reconfigurable digital receiver design and application for instantaneous polarimetric measurement,* (2011).

[11] S. Kullback and R. Leibler, *On information and sufficiency,* (1951).

[12] V. Karnychev, V. A. Khlusov, L. Ligthart, and G. Sharygin, *Algorithms for estimating the complete group of polarization invariants of the scattering matrix (sm) based on measuring all sm elements,* (2004).

[13] J. Huynen, *Phenomenological theory of radar targets,* (1970).

[14] S. Cloude and E. Pottier, *An entropy based classification scheme for land applications of polarimetric sar,* (1987).